

THESIS

NEAR-CLOUD AEROSOL RETRIEVAL AND THREE-DIMENSIONAL RADIATIVE  
TRANSFER USING MACHINE LEARNING

Submitted by

Chen-Kuang Yang

Department of Atmospheric Science

In partial fulfillment of the requirements

For the Degree of Master of Science

Colorado State University

Fort Collins, Colorado

Fall 2021

Master Committee:

Advisor: Christine Chiu

Christian D. Kummerow

Steven D. Miller

Imme Ebert-Uphoff

Copyright by Chen-Kuang Yang 2021

All Rights Reserved

## ABSTRACT

### NEAR-CLOUD AEROSOL RETRIEVAL AND THREE-DIMENSIONAL RADIATIVE TRANSFER USING MACHINE LEARNING

According to the most recent report of the Intergovernmental Panel on Climate Change, aerosols remain one of the largest sources of uncertainty in estimating and interpreting the Earth's changing energy budget. To reduce the uncertainty, an advanced understanding of aerosol optical properties and aerosol-cloud interaction is needed, which has largely relied on (but is not limited to) passive satellite observations. Current aerosol retrieval methods require a separation between cloud-free and cloudy regions, but this separation is often ambiguous. Three-dimensional (3D) cloud radiative effects can extend beyond the physical boundaries and enhance the reflectance in adjacent cloud-free regions as far as 10 km from clouds. Aerosol optical properties cannot be accurately retrieved without considering the 3D cloud radiative effect in this so-called "twilight" or "transition" zone, which denotes the area between cloud-free and cloudy regions. Indeed, most contemporary retrievals discard these regions, making it impossible to estimate the aerosol radiative effects in this zone. To help break the deadlock, 3D cloud radiative effects must be incorporated into the retrieval methods, and two approaches are proposed in this work, both leveraging machine learning techniques.

The first approach accounts for 3D cloud radiative effects by building a 3D shortwave radiative transfer emulator as the forward model for the retrieval methods. Our emulator was trained by cumulus scenes generated from large eddy simulations and radiation fields calculated from 3D radiative transfer, to predict downward and upward flux profiles at a 500 m horizontal

resolution and 30 m vertical resolution. From a case drawn from the testing dataset, our emulator captures the spatial pattern of the surface downwelling flux (e.g., shadows and illuminations), and the associated PDF has a remarkable similarity to the synthetic truth. In addition, compared to 1D calculation, our 3D emulator improves the root-mean-square-error by a factor of 6. For the flux and heating rate profiles, our emulator is much superior to the 1D calculation for the cloudy column. The application of this 3D radiative transfer emulator to numerical weather modeling or large-eddy simulations type of model is beyond the scope of the current work to develop an aerosol retrieval algorithm, but the possibility exists to do so.

While the promising results from the emulator make it possible to conduct 3D RT retrieval methods, this approach still faces ambiguity in separating cloud-free and cloudy pixels. Here, we present a new retrieval algorithm for aerosol optical depth (AOD) in the vicinity of clouds which contains two unique features. First, it does not require pre-separation of aerosols and clouds. Second, it incorporates 3D radiative effects, allowing us to provide accurate aerosol retrievals near clouds. The AOD retrieval uncertainty of this method in the cloud-free region is  $(0.0004 \pm 4\% \text{ AOD})$ , which is much better than the  $(0.03 \pm 5\% \text{ AOD})$  retrieval uncertainty in NASA Aerosol Robotic Network (AERONET). This method shows skill of predicting AOD over the near-cloud regions, and its validity was confirmed by using one of the explainable artificial intelligence methods to demonstrate that the model's decisions are supported by radiative transfer theory. Finally, a case study using MODIS observations shed light on how this new method can be applied to real world observation, possibly leading to new scientific insight on aerosol structure and aerosol-cloud interaction.

## ACKNOWLEDGEMENTS

The journey in the past two years has been full of all kinds of feelings. Living in a new country and away from my family has been a big adjustment for me. But looking back from now, I am glad that I decided to leave my comfort zone and start my career at a place like Atmos, CSU that I can grow the most.

“It takes a village to raise a child”, and it is also true that it takes a lot of people’s support for me to be where I am at now. I want to thank my advisor, Christine Chiu, for her endless and tireless support. She not only taught me how to do research but, more importantly, how to become a better person. It has been an absolute joy to work with her on different projects, and through her, I learned that “the sky is the limit”. I cannot wait to start my Ph.D. and see what good science we can do in the future.

I would also like to thank my collaborators from different academia. The people from NASA Goddard, Alexander Marshak, Tamas Varnai, and Guoyong Wen to bring me into their project and all the great discussions we had during our monthly meetings. Also, Graham Feingold from NOAA CSL provided us with the large-eddy simulations and taught me a lot of insights on cloud microphysics. It is my pleasure to work with these prestigious scientists and learn from them.

Last but not least, I would like to thank my girlfriend, Danni, for always being there when I needed her. Her caring and encouragement motivate me every day, especially during the pandemic. Also, my family has been the best cheerleading in my life, that they always accept who I am and support me in all kinds of ways.

## TABLE OF CONTENTS

ABSTRACT.....	ii
ACKNOWLEDGEMENTS.....	iv
CHAPTER 1: INTRODUCTION.....	1
1.1. Overview .....	1
1.2. Research in this thesis .....	5
1.2.1. 3D Radiative transfer emulator.....	5
1.2.2. A machine-learning based method for retrieving aerosol properties near clouds ....	8
1.3. Outline of the thesis.....	9
CHAPTER 2: 3D SHORTWAVE RADIATIVE TRANSFER EMULATOR.....	10
2.1. Cloud and radiation fields for emulators.....	11
2.2. 3D Convolutional Neural Network .....	16
2.3. Evaluation metrics.....	18
2.4. Results .....	18
2.4.1. Performance of shortwave downwelling flux at the surface.....	18
2.4.2. Performance of flux profiles .....	24
2.4.3. Error statistics for all grid points .....	27
CHAPTER 3: RETRIEVING AEROSOL OPTICAL DEPTH IN THE VICINITY OF CLOUDS USING MACHINE LEARNING TECHNIQUES .....	29
3.1. The Prototype Convolutional Neural Network .....	29
3.1.1. The training and configuration .....	29
3.1.2. The performance.....	34
3.2. A case study using MODIS observations.....	40
CHAPTER 4: SUMMARY AND FUTURE WORK.....	43
4.1. Summary .....	43
4.2. Future work .....	46
REFERENCES .....	49
APPENDIX A.....	60
APPENDIX B.....	62

## CHAPTER 1: INTRODUCTION

### 1.1. Overview

Clouds are a critical component of Earth's climate system for determining the radiation budget and hydrological cycle. The complexity of their nature and interactions with aerosols, precipitation, and radiation remains a large source of uncertainty in quantifications of cloud feedback and aerosol radiative forcing (Forster, et al., 2021). As pointed out by the 2017 NASA Decadal Survey (ESAS, 2017; S-6 and Page 3-59), to reduce the uncertainty in climate change predictions, knowledge of clouds and aerosol properties and processes needs to be advanced.

To date, observations of clouds and aerosols have largely relied on passive satellite measurements. Specifically, daytime shortwave reflectance measurements from satellites have played an important role in providing optical depth and particle size retrievals of clouds and aerosols. These retrievals require a separation between cloud-free and cloudy regions, which are often performed through sophisticated cloud screening procedures. Such separations, however, are ambiguous (Charlson et al, 2007; see Figure 1.1). Additionally, Koren et al. (2007) showed that the optical influence of clouds, due to three-dimensional (3D) radiative effect, can extend far beyond the cloud physical boundaries (see Figure 1.2c). Their optical influence is also evident in 10-year measurements from the Moderate Resolution Imaging Spectroradiometer (MODIS) over a region of the Northeast Atlantic Ocean, showing that clouds can enhance reflectance in cloud-free regions as far as 10 km from clouds (Várnai and Marshak, 2009). Since most retrieval methods are one-dimensional (1D) and thus ignore 3D radiative effects, they cannot account for the enhancement in reflectance. Consequently, pixels influenced by 3D cloud radiative effects are discarded for retrievals of both clouds and aerosols. The region between cloud-free and

cloudy areas, in which these discarded pixels are located, is referred to as the “twilight” or “transition” zone in Koren et al. (2007).

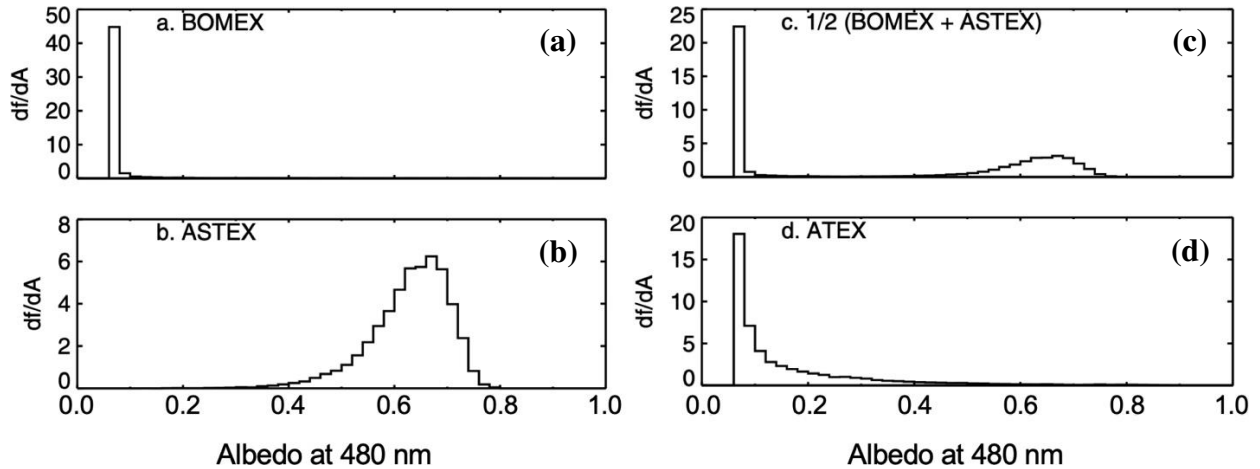


**Figure 1.1.** Probability density functions (PDFs) of albedo at 480 nm from large eddy simulations for (a) trade cumulus with 7% cloud cover during the Barbados Oceanographic Meteorological Experiment (BOMEX), (b) marine stratocumulus with 100% cloud cover during the Atlantic Stratocumulus Transition Experiment (ASTEX), (c) average of BOMEX and ASTEX cloud fields, and (d) trade cumulus with ~54% cloud cover during the Atlantic Trade wind EXperiment (ATEX). Since (c) is the average of (a) and (b), the resulting cloud cover is about 53%, which is nearly the same as that in (d). Although cloud covers in (c) and (d) are the same, their albedo PDF are distinctly different. (c) has a clear bimodal distribution, easy to separate nearly cloud-free and cloudy regions, while (d) has a rather continuous distribution and lacks a clear cut for separating cloud-free and cloudy regions. This figure is taken from Charlson et al (2007).

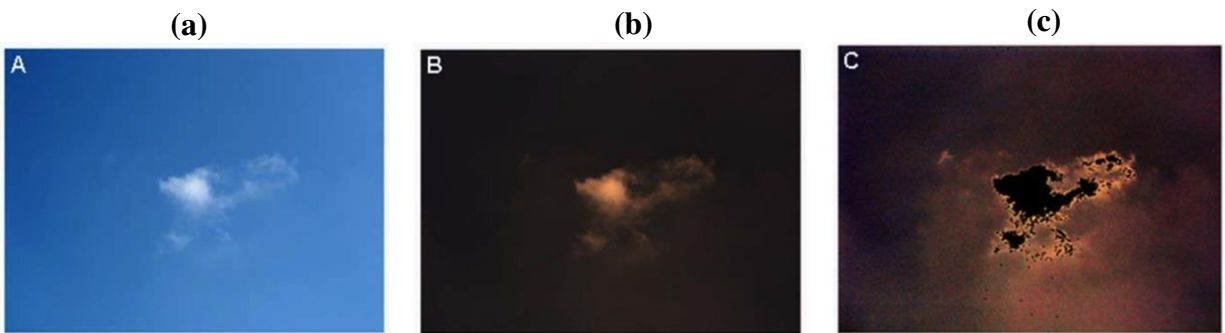


**Figure 1.2.** (a) A picture of a cloud. (b) is the same as (a) but blocking out the background light. (c) is the same as (b) but further obscuring strong scattered light from the cloudy part. As shown in (c), the surrounding areas near clouds are brighter than those far away clouds, demonstrating the optical influence of clouds beyond their physical boundaries. This figure is taken from Koren et al. (2007).

Transition zones are ubiquitous in real-world 3D environments; Várnai and Marshak (2011) estimated that ~50% of cloud-free pixels over ocean are within 4–5 km of low-topped clouds, based on measurements from MODIS and Cloud-Aerosol Lidar with Orthogonal Polarization (CALIOP). Near clouds, aerosol properties can be distinctly different from those far from clouds due to hygroscopic growth, new particle formation, and chemical processing of solutes in clouds that dissipate (Hoppel et al., 1986; Twohy et al., 2002, 2009). Based on aircraft measurements over the Indian subcontinent, Konwar et al. (2015) reported that the concentration of near-cloud aerosols can be enhanced by 81% and their effective diameter can increase by a factor of 2 due to the high humidity environment near clouds. Similarly, Várnai et al. (2017) also showed a 30–50% increase in aerosol optical depth (AOD) in cloudier regions from satellite observations, and Tackett and Di Girolamo (2009) found that an aerosol size distribution with reduced aerosol concentration, increased median radius, and reduced width would best explain the observed enhancement near clouds in backscatter signals of CALIOP. While the finding in enhanced AOD near clouds appears robust, the change in aerosol particle size depends on the underlying processes. For example, using measurements from the NASA Aerosol Robotic Network (AERONET), Eck et al. (2014) observed a size increase in fine mode aerosols in some cases, due to humidification and/or cloud processing, but also a size decrease in other cases due to new particle formation and/or cloud processing.

Since there is no appropriate aerosol retrieval near clouds in passive satellite products, it is challenging to quantify the radiative effects of the transition zone. Eytan et al. (2021) and Jahani et al. (2021) bypassed the need for knowledge of aerosol and cloud properties, calculating the longwave radiative effects by comparing radiation measurements between cloud-free regions and the transition zone. They used broadband flux measurements from the Clouds and the

Earth's Radiant Energy System (CERES) sensor and infrared radiance from MODIS, respectively, and in each case found a  $\sim 0.8 \text{ W m}^{-2}$  of longwave radiative effects for the transition zone. The positive value suggests that the transition zone has a warming effect on the Earth, likely because the enhanced AOD increases absorption, raises the emission height, and then reduces the outgoing emission to space. Based on the recent effective radiative forcing estimate of  $2.16 \pm 0.26 \text{ W m}^{-2}$  (IPCC AR6) for a change in  $\text{CO}_2$  concentrations from 278 ppm in 1750 (pre-industrial) to 410 ppm in 2019 (at present),  $0.8 \text{ W m}^{-2}$  is equivalent to the radiative forcing from increasing  $\text{CO}_2$  concentrations by  $\sim 50$  ppm, which is  $\sim 37\%$  of the  $\text{CO}_2$  concentration increase since the pre-industrial period. Thus the transition zone effect of aerosols should not be ignored.

Up to now, there are very few attempts to estimate the shortwave (SW) radiative effects of the transition zone. Twohy et al. (2009) combined properties of humidified aerosols from aircraft measurements with statistics of the distance of cloud-free regions to clouds from CALIOP observations, finding that the SW aerosol direct radiative effect of the transition zone can be 35–65% larger than cloud-free regions far from clouds. These estimates have been mainly focused on the humidification effects on aerosols. Similarly, if the enhanced reflectance in passive satellite observations is attributed entirely to humidified aerosols, the reflected SW flux at top of the atmosphere (TOA) is larger by  $\sim 6 \text{ W m}^{-2}$  in the cloud-free regions within 5 km from clouds, compared to those far away from clouds (Várnai and Marshak, 2014). In contrast, if the enhanced reflectance is entirely attributed to undetected cloud droplets, the increase in reflected SW flux is  $\sim 3.4 \text{ W m}^{-2}$ , which is reduced by a factor of  $\sim 2$  compared to the first attribution. Unfortunately, the estimates in Várnai and Marshak (2014) are not the same as the radiative

effect of the transition zone, because the reflectance enhancement due to 3D radiative effects has not been removed.

## **1.2. Research in this thesis**

To improve understanding of aerosol properties in the transition zone and better quantifying their SW radiative effects. 3D radiative transfer (RT) is the key, which forms the two main work chapters for this thesis.

### *1.2.1. 3D Radiative transfer emulator*

First, as concluded by Stap et al. (2016) and Spencer et al. (2019), the 3D radiation interactions between clouds and the surrounding clear air and aerosols appear to be the main source for the enhanced reflectance near clouds, and a retrieval method must account for 3D cloud radiative effects to substantially improve aerosol retrievals near clouds. Incorporating 3D radiative effects, however, is not trivial. To understand this issue, let us briefly explain how existing aerosol retrieval methods work. Typically, AOD retrieval methods use a few predefined aerosol models. Based on these models, lookup tables of reflectance are pre-calculated for a range of AOD under a set of sun-viewing geometry and surface reflectance conditions using 1D RT model. Retrievals are then made by searching the best estimate that corresponds to the best agreement between the observed reflectance and the value in lookup tables considering all the available wavelengths of observation simultaneously. For convenience, we call these lookup tables used in existing retrieval methods as 1D RT lookup tables.

There are generally two approaches to account for 3D effects in this type of retrieval framework. The first approach assumes 1D RT but tries to account for the 3D effect by estimating and removing it from the measurements before interrogating the 1D RT lookup tables. For example, aerosol retrievals can be improved by using spectral reflectance ratios that are less

susceptible to 3D effects (Kassianov et al., 2009), but this method does not explicitly remove 3D effects and still cannot work for pixels near clouds. In contrast, Wen et al. (2013, 2016) estimated the 3D radiative effects by calculating the reflectance enhancement induced by near-by clouds and their interactions with the molecular layer above, and then subtracted the 3D effects from the observed reflectance for aerosol retrieval. Since the kind of correction is based on a simple set up, the method requires prior information on cloud height and does not account for more complex morphology situations, e.g., aerosol layers above clouds.

The second retrieval approach is to incorporate 3D RT in the forward model. This method requires iterations during the process of finding the best estimate of aerosol properties, with 3D RT calculations required at each iteration. Since 3D RT is extremely expensive, numerical methods of computational speed acceleration are necessary. To account for the horizontal inhomogeneity of clouds, earlier studies (e.g., Gabriel and Evans, 1996; Várnai and Davies, 1999) calculated the radiative transfer using a tilted column along the direct solar beam. This change corrects the first-order errors introduced by the independent column approximation (ICA; called independent pixel approximation (IPA) in Cahalan et al., 1994), in which 1D plane-parallel RT is applied to individual columns. These methods, however, are still not a true 3D RT, because they do not consider horizontal photon transport. As shown in Marshak et al. (1995), horizontal photon transport leads to a cloud radiance field that is smoother than the corresponding cloud field on small scales, so-called “radiative smoothing process”. To incorporate the effects of horizontal photon transport so that the observed radiance field can be properly reproduced, Marshak et al. (1998) proposed a “Nonlocal Independent Pixel Approximation”, and applied a smoothing kernel to the radiance field computed from ICA. These methods and concepts are further combined by Wapler and Mayer (2008) and Wissmeier

et al. (2013), showing good results in surface solar flux calculations for numerical weather prediction (NWP) and Large Eddy Simulation (LES) models. In general, the error is improved by a factor of 4 compared to the 1D RT for an oblique solar zenith angle of 60 degrees.

Unlike the methods above that consider a smoothing kernel, Hogan and Shonk (2013) introduce explicit terms that represent the photon exchanges laterally between the clear and cloudy regions in the two-stream radiative transfer scheme. Another major advance was made by Jakub and Mayer (2015), expanding the treatment of diffuse radiation from two-streams to ten-streams, and three streams for direct radiation. When coupling individual homogeneous grid points to form a set of equations for this ten-stream system, the coefficients of the equations are pre-calculated to improve the speed of the solver dramatically. Overall, the ten-stream scheme improves the errors of heating rates by a factor of five compared to ICA, but the increase in computational time by a factor of 15 compared to ICA two-stream scheme remains a concern for operational uses.

In this thesis, we explore the potential of machine learning techniques for 3D RT. The use of machine learning for accelerating RT is not a new concept. In fact, many other machine-learning based emulators have been built (Chevallier et al., 1998, 2000; Krasnopolsky et al., 2005, 2006, 2010; Belochitski et al., 2011; Pal A et al., 2019; Reichstein et al., 2019; Roh and Song, 2020) for weather forecast and climate models, but they are all 1D based.

In Chapter 2, we introduce our own 3D SW RT emulators based on machine learning techniques. We have built emulators for computing radiance and flux but will focus only on results in downward and upward fluxes at all layers and heating rate profiles in this thesis. Specifically, we address the following questions:

- How well do 3D SW RT emulators capture the spatial distribution of surface radiation for a highly inhomogeneous cumulus regime?
- What are the errors in predictions of flux and heating rate? How are these errors compared to those from 1D RT calculations?

### *1.2.2. A machine-learning based method for retrieving aerosol properties near clouds*

While the work in Chapter 2 makes it possible to directly incorporate 3D RT in AOD retrievals, these methods will eventually face the same ambiguity in separating cloud-free and cloudy pixels. Although machine learning techniques have been increasingly used in satellite observations for cloud screening (Wang et al., 2020), the nature of ambiguity has not changed, and the resulting classification will suffer from the same issue. Motivated by Okamura et al. (2017) who applied Convolution Neural Network (CNN) to 3D cloud retrievals, we aim to build a machine-learning based method for retrieving aerosol properties, particularly near clouds. The flexibility of CNN allows us to incorporate not only 3D effects, but also potential humidification effects on aerosol properties. Specifically, we plan to address the following questions:

- How well does the machine-learning based method retrieve AOD, particularly in the vicinity of clouds?
- Are results from explainable AI techniques for near-cloud AOD predictions supported by our understanding of radiative transfer?
- How well does the machine-learning based method perform in real world applications, compared to exiting operational products?

### **1.3. Outline of the thesis**

The thesis is organized as follows. In Chapter 2, we detail how our 3D emulators were built. The components include the input cloud and aerosol fields from LES outputs, the radiative transfer used to compute broadband SW fluxes, and the configuration of the CNN. Performance in snapshots of surface downwelling flux are discussed. Overall error statistics of downwelling and upwelling fluxes at all layers and the corresponding heating rate profiles are presented and compared to those from the existing fast 3D RT schemes.

In Chapter 3, we detail our new retrieval method for AOD. A prototype CNN is presented to prove the concept. Importantly, it is used to explain what the CNN learns for AOD predictions near clouds. Additionally, the prototype CNN will be applied to MODIS observations for a case study. Since current MODIS retrievals work well for cloud-free pixels far away from clouds, they serve as a reference for evaluating our CNN.

Finally, in Chapter 4, key findings from the two work chapters will be summarized, and thoughts on future work will be provided.

## CHAPTER 2: 3D SHORTWAVE RADIATIVE TRANSFER EMULATOR

The magnitude of 3D cloud effects depends on several factors including solar zenith angle (SZA), cloud types, cloud distribution, and the underlying surface reflectance. As shown in Fig. 2.1., the 3D cloud effects at TOA increase with increasing SZA and are most significant for cumulus clouds. Hence, the 3D RT emulators introduced in this chapter are specifically designed for such conditions and cloud types in mind.

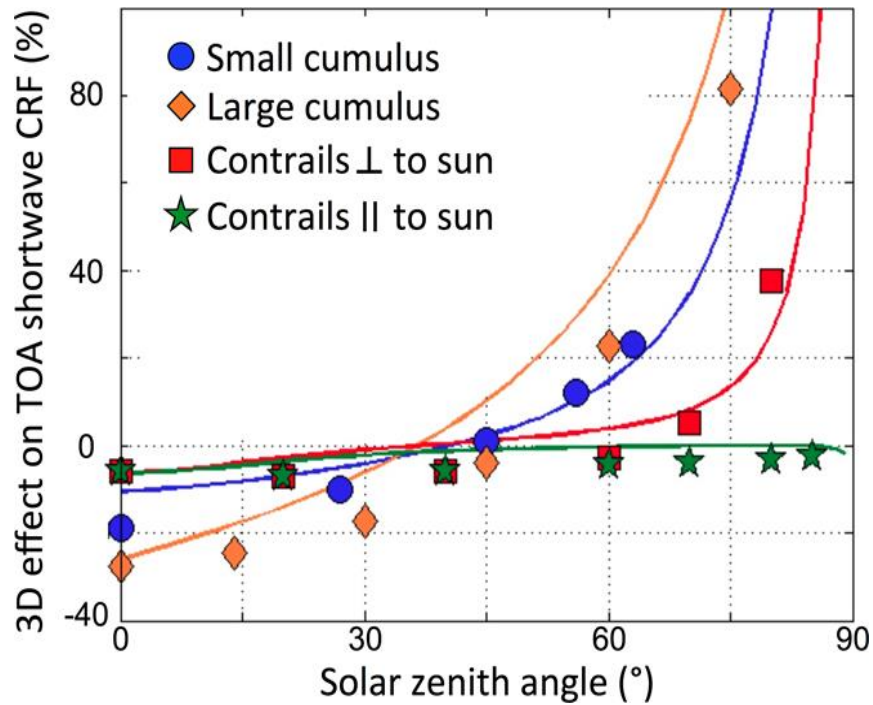


**Figure 2.1.** The effect of 3D radiative transfer on shortwave TOA cloud radiative forcing (CRF) versus solar zenith angle for cumulus clouds and contrails, using full 3D radiative transfer codes (symbols) and the scheme described in Hogan and Shonk (2013). CRF is defined as the difference between the clear-sky and cloudy-sky upwelling shortwave radiation at TOA, which is negative except over very reflective snow-covered surfaces. The “small cumulus” results are from Benner and Evans (2001) and the “large cumulus” from Pincus et al. (2005). The contrail results are from Gounou and Hogan (2007). Adapted from Hogan and Shonk (2013).

## 2.1. Cloud and radiation fields for emulators

The U.S. Department of Energy’s Atmospheric Radiation Measurement (ARM) user facility recently initiated the Large-Eddy Simulation ARM Symbiotic Simulation and Observation (LASSO) activity. LASSO has routinely provided simulations at the Southern Great Plains (SGP) site in Oklahoma for days that meet the criteria for a shallow convection regime (Gustafson et al., 2020). The regime was chosen because shallow cumuli play an important role in regulating both the thermodynamic and kinematic atmospheric structure (Drueke et al., 2020), per Fig. 2.1, and are challenging for models to simulate (Nam et al., 2012). Simulations were performed with various forcing datasets, resolutions, and cloud microphysics schemes using either the Weather Research and Forecasting (WRF) Model (Skamarock et al., 2008) or the System for Atmospheric Modeling (SAM) (Khairoutdinov and Randall, 2003). Although simulations are not reality, they provide a wide range of possible cloud scenes, required for characterizing 3D cloud radiative effects. These simulations serve as input to the 3D emulator. It would be ideal to establish an input dataset from observations, but there is no routine 3D cloud observation dataset yet and such a dataset would also contain retrieval uncertainty.

LASSO provides 30 cases in April–September 2017. Each simulation started early morning to late afternoon and produced 3D cloud fields every 10 min. For each day, simulations were compared to ARM vertically pointing cloud observations, and the corresponding skills were computed for various model configurations. Specifically, we used “cloud\_mask\_2d\_net\_skill” that combines information on the relative mean bias and the Taylor skill score to select the best set of simulations for emulators. We have found that simulations from the Thompson microphysics scheme tend to have higher scores consistently, and thus have only included simulations from this specific scheme. Since shallow cumulus at SGP typically

initiates around 10–11 am local time, we excluded scenes prior to 10 am. We also excluded scenes with cloud fractions less than 0.2 or larger than 0.8, since their 3D effects tend to be small. Following these selection rules, we collected 279 snapshots from those 30 cases. However, we only managed to run 127 snapshots for the emulator since we have used up all the free resources (see Appendix B for more detail).

Each snapshot has a domain size of 25 km x 25 km x 4.5 km. Examples of snapshots in Figure 2.2 illustrates the variety of cloud sizes. For example, Figure 2.2a represents a field with scattered small cumulus clouds (i.e., thickness less than 300 m), while Figure 2.2b represents a field with larger cumulus. Based on a snapshot-by-snapshot basis (see Figure 2.3), the mean cloud geometric thickness ranges between 80 and 360 m, and cloud base and cloud top heights vary significantly among all the snapshots.

LASSO cloud fields provide information on liquid water content. For radiation calculations, cloud droplet size information is also needed. Assuming a lognormal cloud droplet size distribution, cloud water content relates to effective radius via the following equation:

$$W_c = \frac{4\pi\rho_w}{3} N_c r_e^3 \exp(-3\sigma^2), \quad (2.1)$$

where  $W_c$  is the cloud water content,  $N_c$  is the cloud droplet number concentration,  $r_e$  is the cloud effective radius,  $\sigma$  is the geometric standard deviation of the size distribution, and  $\rho_w$  is water density. Based on in-situ measurements at SGP, we assume  $N_c$  of  $400 \text{ cm}^{-3}$  (Vogelmann et al., 2012; Lim et al., 2016) and  $\sigma$  of 0.3 (Miles et al., 2000). The resulting distribution of  $r_e$  peaks at 4–7  $\mu\text{m}$ , which is typical for the SGP site (Kim et al., 2003; Sengupta et al., 2003).

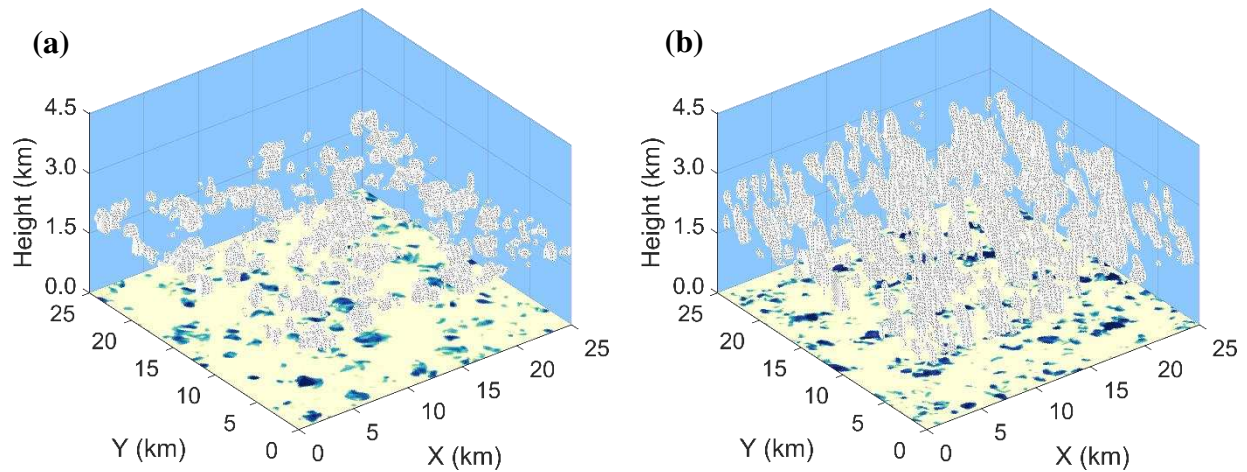


**Figure 2.2.** Examples of snapshots for cloud fields with (a) scattered shallow cumuli and (b) large cumuli. Cloud water content is plotted as grey iso-surface. Downwelling shortwave broadband flux at surface is plotted in color, in which yellow represents higher fluxes associated with clear sky and blue represents lower fluxes associated with shadows cast by clouds.

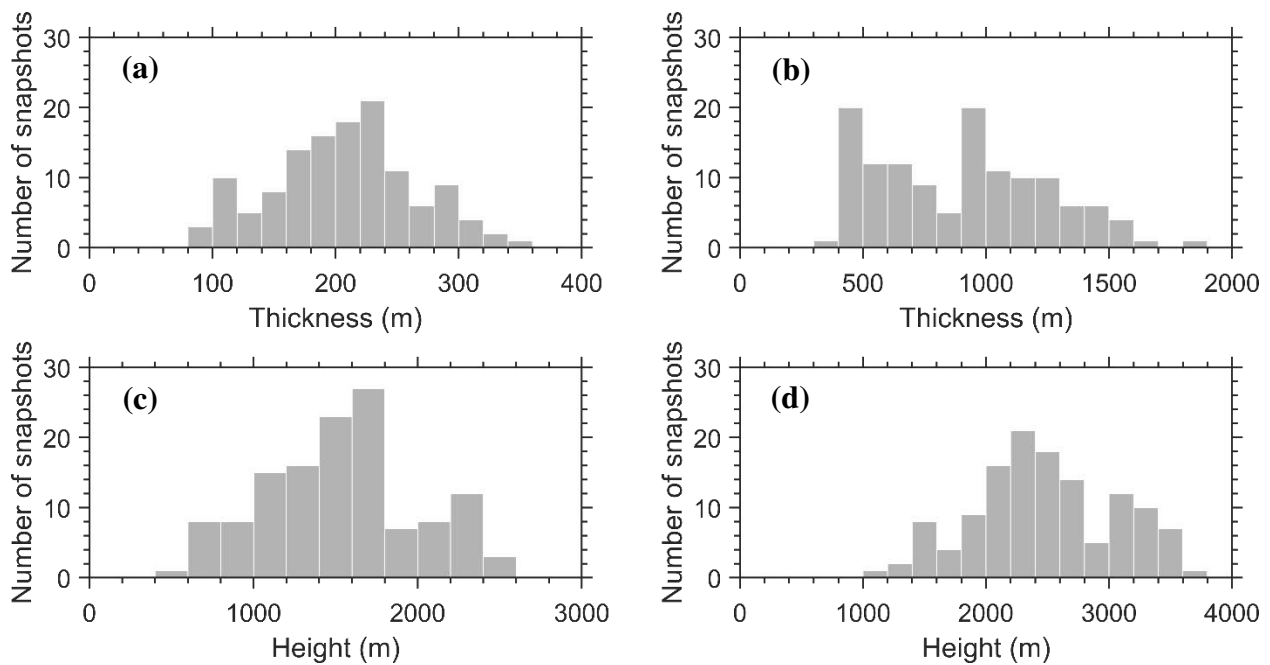


**Figure 2.3.** Snapshot-based statistics. Histograms of (a) mean cloud thickness, (b) maximum cloud thickness, (c) minimum cloud base height, and (d) maximum cloud top height.

The upwelling and downwelling fluxes in the SW were computed using the Spherical Harmonic Discrete Ordinate Method (SHDOM; Evans, 1998) under a 3D environment. Details of several key components are provided here. First, we used the solar spectral irradiance of  $1361 \text{ W m}^{-2}$  (Matthes et al., 2017). The solar azimuth angle is  $180^\circ$  clockwise from the north (i.e., the

sun is in the south), and we include two runs with SZA of  $0^\circ$  and  $60^\circ$  to ensure that the emulators work as expected for both cases. Second, Rayleigh (molecular) scattering is included, and a Lambertian surface is assumed with an albedo of 0.05. A homogeneous sulfate aerosol layer with AOD of 0.15 at 550 nm from the surface to 2 km height is included based on the climatology reported in Wu et al. (2021) for the SGP site. Third, since the maximum cloud top is lower than 4.5 km in our snapshots (Figure 2.3d), we took LASSO output up to 4.5 km (i.e., 150 levels with a vertical resolution of 30 m), and then added six more layers in SHDOM to incorporate surface information and atmospheric information above 4.5 km to 15 km for RT calculations. The temperature and water vapor profiles are taken from LASSO output and averaged over a snapshot, while  $O_3$  concentration is based on the standard mid-latitude summer atmospheric profile.

Finally, the component that requires most consideration is the gas absorption, mainly because of the required computation. Gas absorption is incorporated through so-called correlated k-distribution. SHDOM has coupled with two commonly used k-distribution schemes: one is from the Rapid Radiative Transfer Model for GCMs (RRTMG; Mlawer et al., 1997) and the other is from Fu and Liou code (Fu and Liou, 1992). For the SW from  $0.2 \mu\text{m}$  to  $4 \mu\text{m}$ , RRTMG has 14 bands with 112 spectra intervals in total, while the Fu-Liou code has 6 bands with a total of 54 spectral intervals. Recently, Wu et al. (2021) demonstrated that the derived surface radiation using Fu-Liou code agrees well with ARM observations. Since Fu-Liou code also has fewer spectral intervals compared to RRTMG, which is great advantage for computational purposes, we have used Fu-Liou code in our RT calculations. Additionally, following the recommendation of Q. Fu (personal communication) and the changes made in the NASA

Langley version of code, we divided the first band further to ten bands to calculate the Rayleigh scattering more accurately.

Our 3D calculations were compared to Monte Carlo calculations (provided by J. Gristey) using a LASSO case in 2015 (Gristey et al., 2020). Figure 2.4 shows that the spatial pattern from two methods agree well. Additionally, both show a bimodal PDF, in which the mode with a higher value corresponds to clear skies, and the other corresponds to cloudy skies. There is a difference of  $10 \text{ W m}^{-2}$  in the peak associated with clear skies, which is about 1% error and can be attributed to the different treatment in Rayleigh scattering and interpolations of cloud optical properties between grid points.

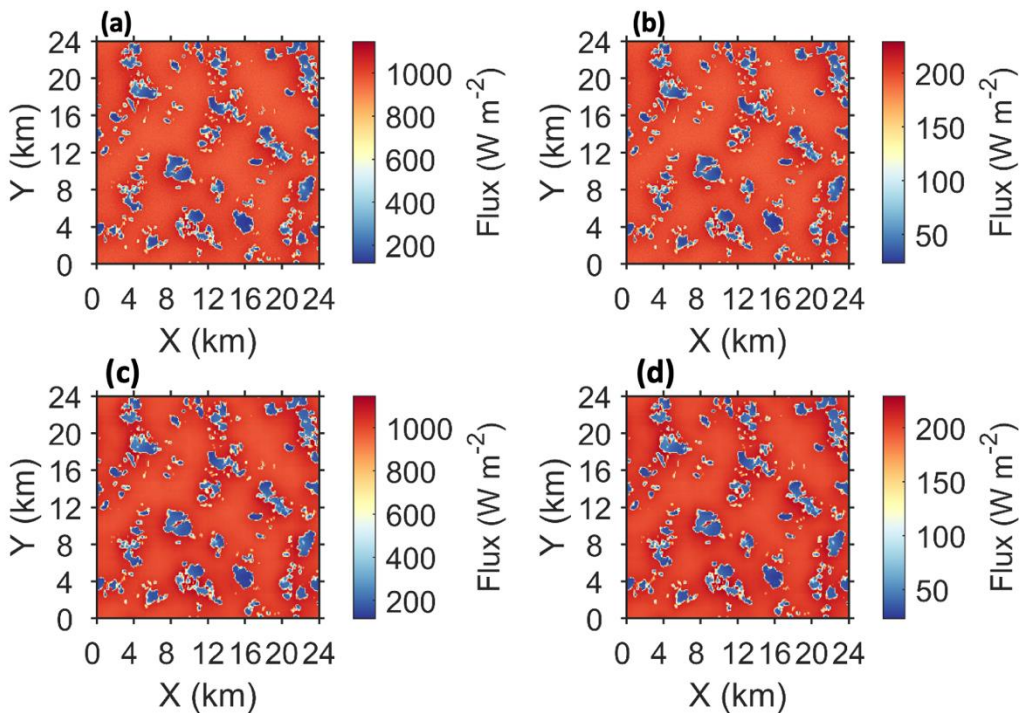


**Figure 2.4.** Comparisons of our SHDOM calculations to Monte Carlo calculations. (a) and (b) are respectively the downwelling and upwelling fluxes from Monte Carlo. (c) and (d) are the same but from SHDOM calculations.

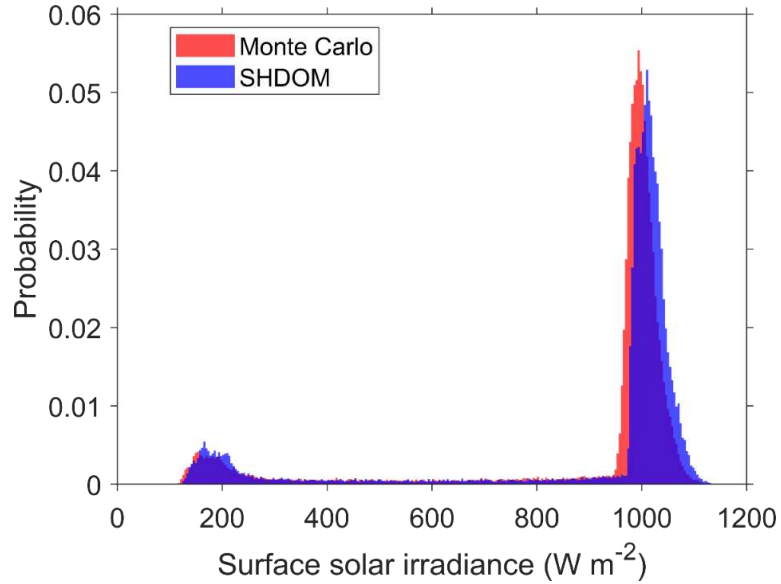


**Figure 2.5.** PDFs of surface downwelling shortwave flux, calculated from Monte Carlo (red) and SHDOM (blue).

## 2.2. 3D Convolutional Neural Network

The cloud and radiation fields generated in Section 2.1 were used to generate our training and testing dataset. As mentioned, both cloud water content and effective radius are critical for determining SW radiation. Hence, our input includes two 3D data pillars – one for cloud water content and the other for effective radius, as shown in Figure 2.6. Since the desired horizontal resolution of the output flux for the emulator is on the scale of 500 m (with the footprint size of MODIS type of sensors and LES model resolution in mind), the input domain needed to be larger than 500 m. Considering that most cloud heights were around 2 – 2.5 km in our input cloud scenes (Figure 2.3), we chose an input size of 7.5 km x 7.5 km x 4.5 km to allow for cloud inhomogeneity along the direct beam to be fully incorporated in emulators especially for a given SZA of 60°. Then, we randomly selected 1,600 pillars with a domain size of 7.5 km x 7.5 km x 4.5 km from the 127 scenes. The resulting sample size was 0.4 M and randomly split into 80% for training and 20% for testing.

Our 3D CNN was built as two convolution layers having 64 and 128 filters, respectively, followed by eight fully connected layers with 1,024 nodes in each layer (see Appendix A for more detail). The convolution calculation was performed only for the two data pillars (i.e., cloud water content and effective radius). Unlike cloud fields, the gas profile is domain-averaged; it is 1D and thus does not need to be included in convolution layers. The gas profile was input into the network before the fully connected layers (see Figure 2.6). We used ReLU (Agarap, 2019) as the activation function at each node across all layers. The input and output values were scaled using the mean normalization (i.e., subtracting the average and then dividing by the dynamical range of the values). Additionally, the training of the network was performed by the Adam optimizer with the loss function defined as the mean squared error between the true value and the prediction.

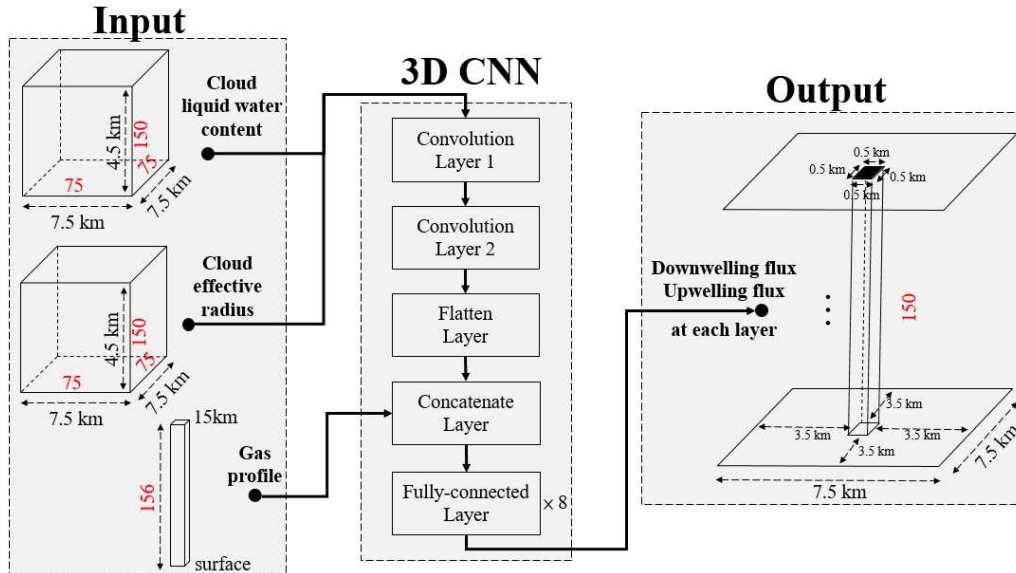


**Figure 2.6.** A diagram showing the configuration of our 3D shortwave radiative transfer emulator. The domain size is labelled in black, while the corresponding number of grid points is labelled in red.

### 2.3. Evaluation metrics

The performance of our 3D emulators is based on the following metrics, which represent the general performance among all the pixels from all testing samples:

$$\text{Error (\%)} = \frac{1}{N} \left[ \sum_{i=1}^N \frac{F_{pred,i} - F_{true,i}}{F_{true,i}} \times 100\% \right] \quad (2.2)$$

$$\text{Absolute Error (\%)} = \frac{1}{N} \left[ \sum_{i=1}^N \left| \frac{F_{pred,i} - F_{true,i}}{F_{true,i}} \right| \times 100\% \right] \quad (2.3)$$

$$\text{Absolute Error (W m}^{-2}\text{)} = \frac{1}{N} \left[ \sum_{i=1}^N |F_{pred,i} - F_{true,i}| \right] \quad (2.4)$$

$$\text{RMSE (W m}^{-2}\text{)} = \left[ \frac{1}{N} \sum_{i=1}^N (F_{pred,i} - F_{true,i})^2 \right]^{\frac{1}{2}} \quad (2.5)$$

$$\text{RMSE (\%)} = \frac{1}{\overline{F_{true}}} \left[ \frac{1}{N} \sum_{i=1}^N (F_{pred,i} - F_{true,i})^2 \right]^{\frac{1}{2}}, \quad (2.6)$$

where the subscript ‘‘true’’ and ‘‘pred’’ represent the truth and the predicted value, respectively.

The subscript ‘‘i’’ denote the *i*th sample, while *N* is the total number of samples. Finally,  $\overline{F_{true}}$  is the average of the true flux from all the samples.

### 2.4. Results

#### 2.4.1. Performance of shortwave downwelling flux at the surface

We first examined whether the 3D RT emulator could reproduce the spatial pattern of surface radiation and the associated PDF. Figure 2.7 shows an example of a scattered cumulus field with cloud fraction of 0.13 at a SZA of 60°. Clouds are located at 1.4 – 2.4 km altitudes with a domain-mean liquid water path (LWP) of 47 g m<sup>-2</sup>. For comparison, surface radiation using 1D RT was included in Figure 2.7b.

Since each pixel (or column) is independent in the 1D setup, all the shadows cast by clouds occur directly beneath the clouds, i.e., the pixels with large LWPs in Figure 2.7a are collocated with the small surface fluxes in Figure 2.7b. In contrast, the 3D RT results in Figure 2.7c show that the shadows are shifted toward the north. In 3D, the shadows appear to be darker, consistent with Figure 2.8 showing that the probability of low fluxes (e.g.,  $100 \text{ W m}^{-2}$ ) increases. Additionally, the inter-cloud regions areas surrounding the shadows appear to be brighter than those in 1D. This leads to a hump at  $\sim 500 \text{ W m}^{-2}$  in the PDF, which is a common feature of 3D radiative effects. The hump is due to the mechanism of downward escape, as illustrated in Figure 2.9. In 1D, photons could only travel up or down in the vertical; in 3D, photons can travel horizontally, allowing them to escape from cloud sides. Since cloud droplets scatter light strongly in the forward direction, the escaped photons move downward and thus enhance surface radiation, as shown in Figures 2.7 and 2.8. The combination of the enhanced downward escape and the increased path introduced by an oblique SZA leads to an increased attenuation in direct beams, which makes the shadows darker in 3D than 1D.

Note that even with the enhanced downward escape, the domain-mean fluxes between 1D and 3D are similar for SZA of  $60^\circ$ ; the difference is only about  $3 \text{ W m}^{-2}$ . This behavior is similar to the finding in Várnai (2010), showing that  $60^\circ$  is close to the point where the sign of the difference in downwelling SW surface fluxes between 3D and 1D changes from positive to negative with increasing SZA, which explains the small difference in domain mean fluxes in our cases.

Compared to the truth 3D radiation field (Figure 2.7c), the prediction from our 3D emulator captures the spatial pattern (Figure 2.7d) and the associated PDF has remarkable similarity to the truth (Figure 2.8c). Additionally, compared to 1D calculations, the error

statistics shown in Table 2.1 suggests that our 3D emulator reduced the errors by a factor of 6 to 14 depending on the metric used in evaluations.

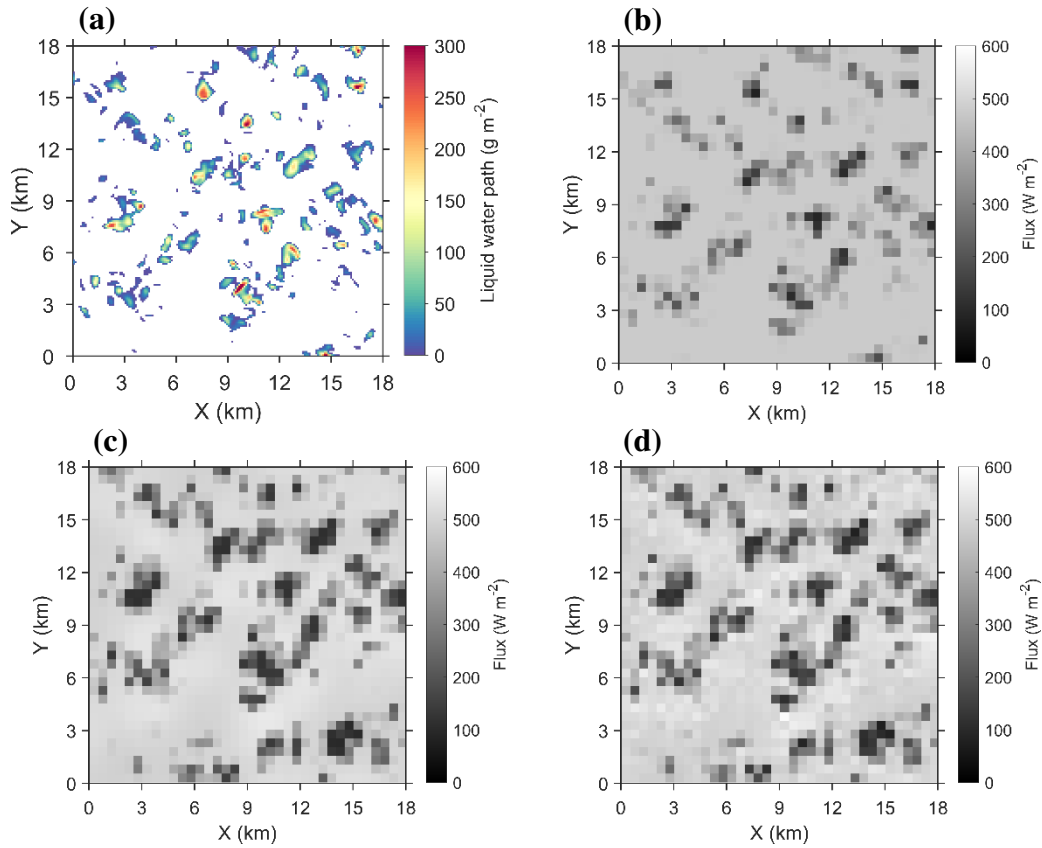


**Figure 2.7.** An example illustrating the performance of our 3D RT emulator in downwelling surface flux. (a) is the liquid water path in the scene. The positive x-direction points to the East, and the positive y-direction points to the North. (b) is the surface fluxes computed from SHDOM in a 1D setup, while (c) is the 3D counterpart with the Sun shining from the South and a SZA of 60°. (d) is the prediction from our 3D emulator.

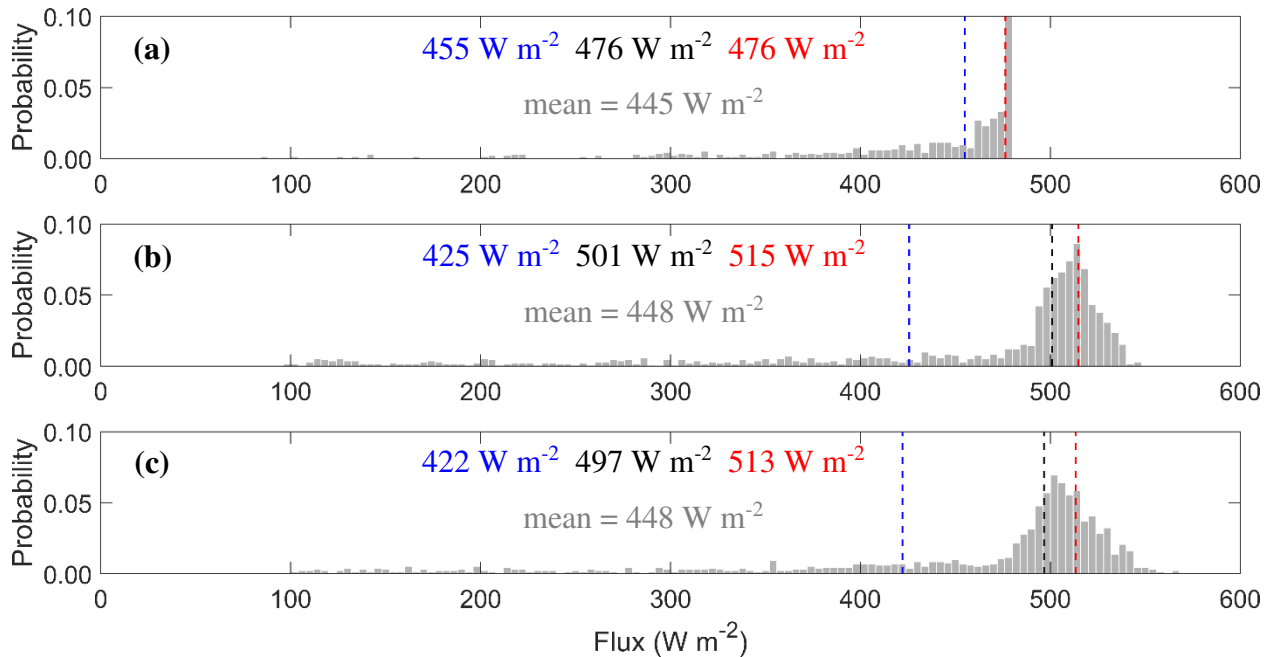


**Figure 2.8.** The probability density function of surface shortwave downwelling fluxes calculated from (a) 1D RT, (b) 3D RT, and (c) the prediction from our 3D emulator for SZA of  $60^\circ$  and an azimuth angle of  $0^\circ$ . The blue, black, and red dashed lines represent the 25th, 50th, and 75th percentiles of the data. The corresponding percentiles (in their own colors) and the means (in grey) are provided in each subplot.

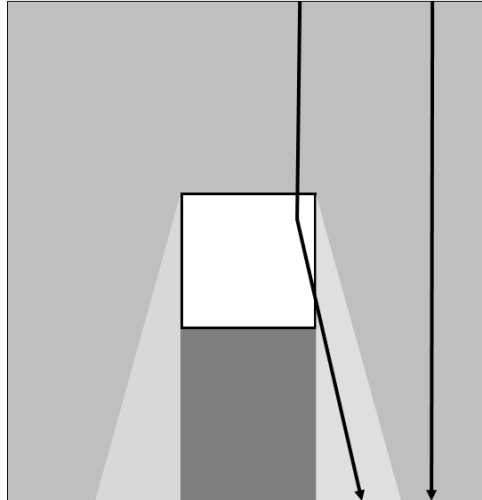


**Figure 2.9.** A schematic illustration of the so-called “downward escape” mechanism. The white square represents clouds, while the black area underneath is the resulting shadow. Arrow at right indicates how photons travel in 1D calculations. Arrow at left represents that photons are scattered and escaped from cloud side, and then move downward reaching the surface. The escaped photons illuminate the surface adjacent to cloud shadows, as shown in light gray in contrast to the dark grey background. Adapted from Hogan and Shonk (2013).

**Table 2.1.** Domain mean error statistics in surface downwelling flux for the scene shown in Figure 2.7.

	Error (%)	Absolute Error (%)	Absolute error ( $\text{W m}^{-2}$ )	RMSE ( $\text{W m}^{-2}$ )	RMSE (%)
<i>Solar zenith angle = 60°</i>					
1D RT	14	34	95	138	31
3D Emulator	0	5	16	22	5
<i>Solar zenith angle = 0°</i>					
1D RT	0.42	8	68	83	8
3D Emulator	0.09	1	12	17	2

We also tested our 3D emulator for a SZA of  $0^\circ$  (i.e., sun directly overhead). Similarly, the emulator reproduced the spatial pattern and the PDF of surface downwelling fluxes (Figures 2.10 and 2.11). The prediction errors were generally reduced by a factor of 4–6 (see Table 2.1). Comparing Figure 2.11b and 2.11c, the locations of the shadows are the same between 1D and 3D results, because the sun is overhead and thus clouds do not cast shadows laterally. It is evident that the areas surrounding the shadows are enhanced in 3D, due to the downward escape mechanism. The enhanced downward radiation leads to an increase of  $22 \text{ W m}^{-2}$  in domain-average flux in 3D and was well captured by our 3D emulator.

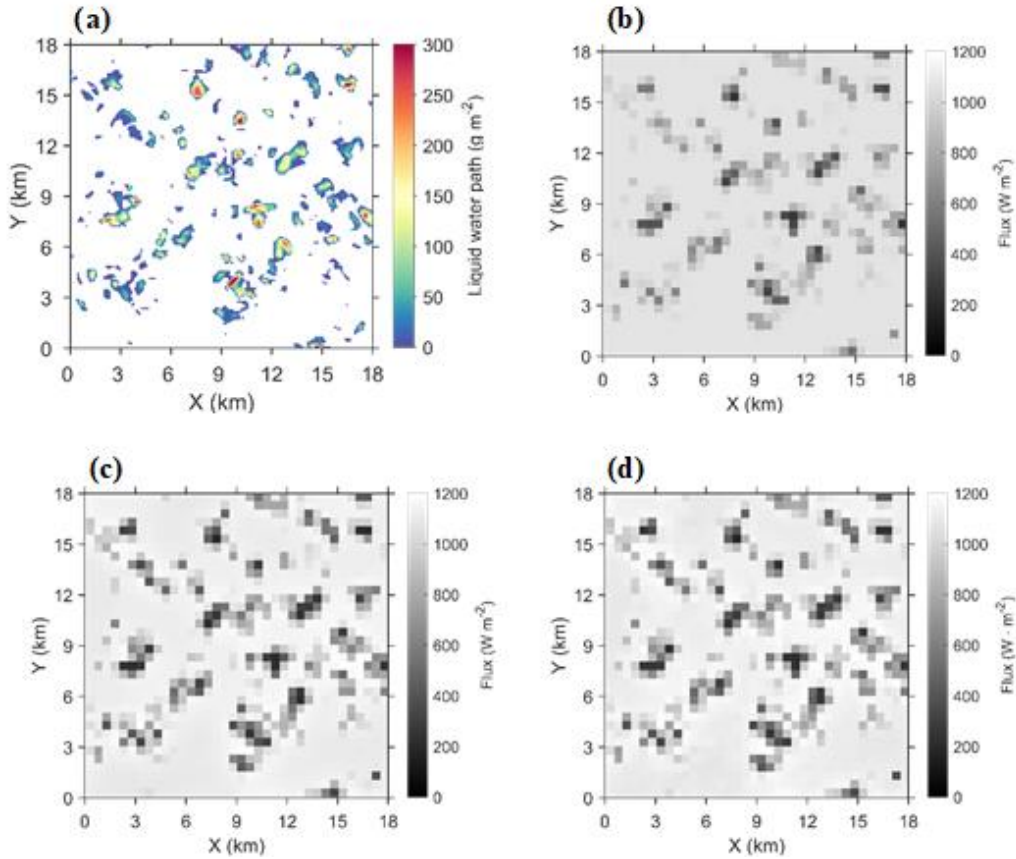


**Figure 2.10.** Same as Figure 2.7 but for SZA of  $0^\circ$ .

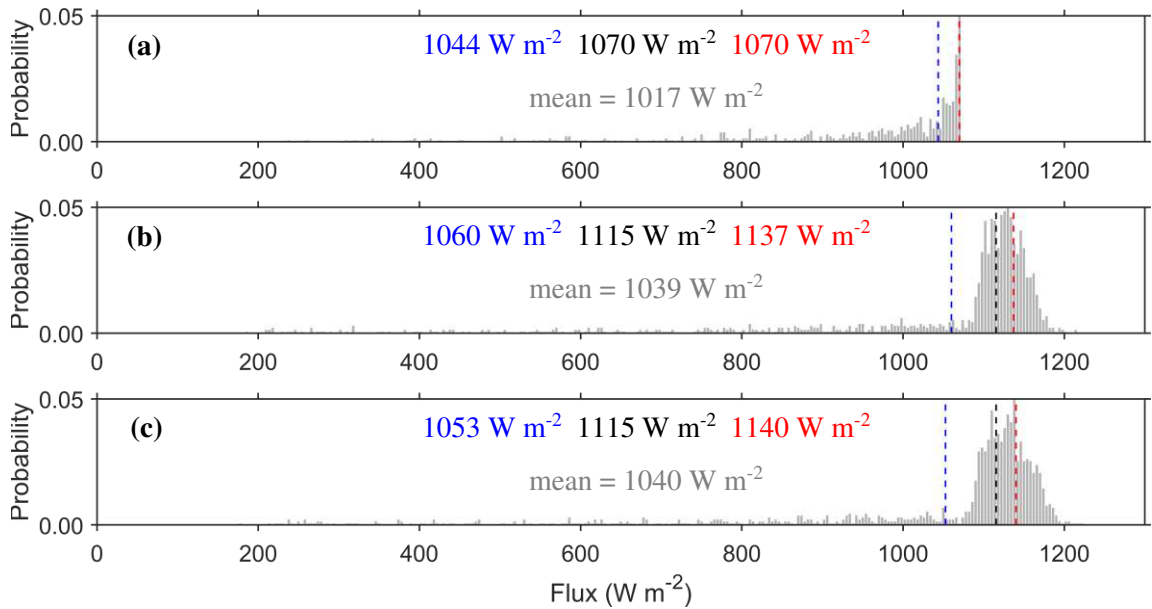


**Figure 2.11.** Same as Figure 2.8 but for SZA =  $0^\circ$ .

### 2.4.2. Performance of flux profiles

Figures 2.12 and 2.13 show examples of flux and heating rate profiles for a cloudy column and a cloud-free column, respectively. In general, the 3D emulator performs well for the cloudy pixel, capturing the variations of the downwelling flux and heating rate profile. In contrast, flux and heating profiles from 1D calculations fail to reproduce the variation in fluxes and the peaks in heating rate profiles. The predicted heating rate profile from our 3D emulator is noisy at altitudes above 1.8 km when the heating rate is small. This noisy behavior is also evident in the cloud-free condition as shown in Figure 2.13.

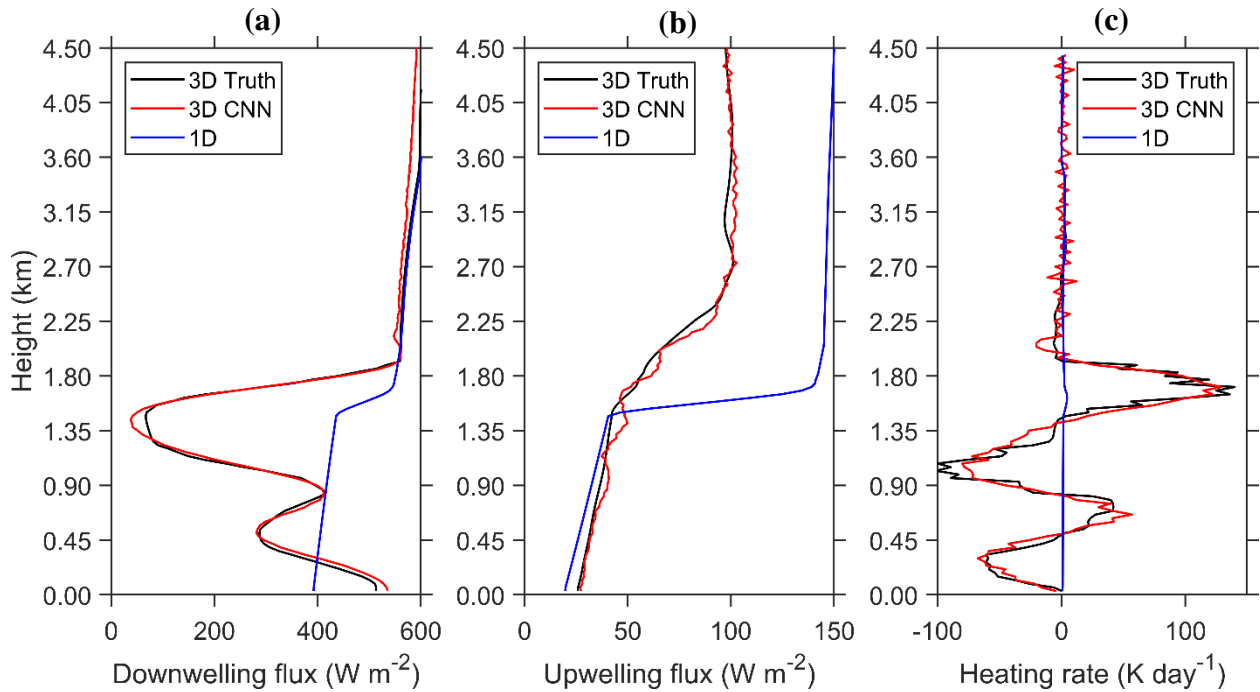


**Figure 2.12.** An example profile of (a) downwelling flux, (b) upwelling flux, and (c) heating rate under solar zenith angle of  $60^\circ$  for a cloudy column.

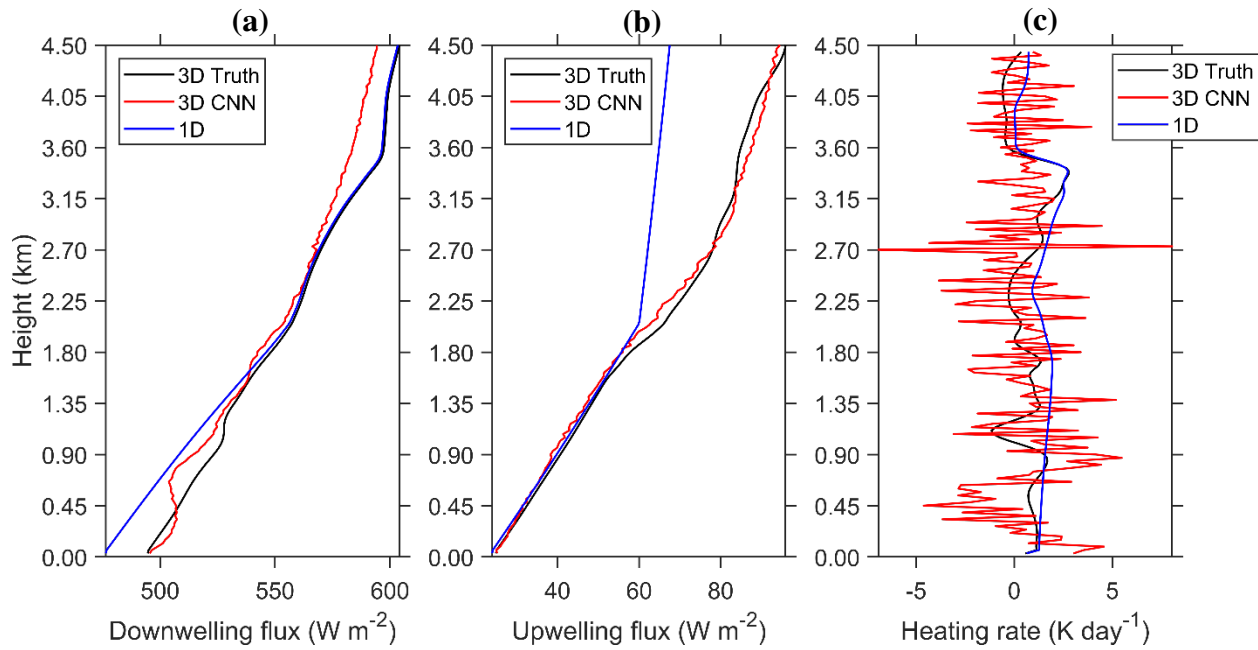


**Figure 2.13.** Same as Figure 2.12 but for a clear-sky column.

The error statistics for these two cases are listed in Table 2.2–2.4. For RMSE in  $\text{W m}^{-2}$ , 3D emulators improve the flux profile prediction dramatically both downwelling and upwelling, especially for cloud columns. 3D emulators also reduce the RMSE in heating rate by a factor of  $\sim 3$  for the cloudy column. Note that since the vertical resolution used here is 30 m, the magnitude of the heating rate is large. RMSE of predictions for atmospheric heating rate from the ten-stream method (Jakub and Mayer, 2015) is about  $33\text{--}64 \text{ K day}^{-1}$ , which is comparable with our RMSE of  $11.5 \text{ K day}^{-1}$ . Figure 2.14 illustrates the link between the error in radiative flux predictions and the error in heating rate predictions. Taking the two layers associated with the largest heating rate error in the cloudy column case, we learned that if the two layers have opposite trend in prediction compared to the truth, e.g., the prediction in downwelling flux is smaller in the upper layer and larger in the lower layer, that could result in a very different net

flux divergence between the truth and the prediction. In this case, the heating rate difference is about 30 K/day.

**Table 2.2.** Errors in downwelling flux at all levels for profiles shown in Figures 2.12 and 2.13.

	Error (%)	Absolute error (%)	Absolute error ( $\text{W m}^{-2}$ )	RMSE ( $\text{W m}^{-2}$ )	RMSE (%)
<i>Cloudy column</i>					
1D RT	56	58	72	137	30
3D Emulator	-2	4	12	14	3
<i>Clear column</i>					
1D RT	-1.01	1.01	5.25	8.32	1.49
3D Emulator	-1.00	1.10	6.22	7.35	1.32

**Table 2.3.** Same as Table 2.2 but for upwelling flux.

	Error (%)	Absolute error (%)	Absolute error ( $\text{W m}^{-2}$ )	RMSE ( $\text{W m}^{-2}$ )	RMSE (%)
<i>Cloudy column</i>					
1D RT	41	49	38	46	65
3D Emulator	3	4	2	3	4
<i>Clear column</i>					
1D RT	-13	13	11	14	22
3D Emulator	-1	3	2	2	3

**Table 2.4.** Same as Table 2.2, but for heating rate.

	Error (%)	Absolute error (%)	Absolute error ( $\text{K day}^{-1}$ )	RMSE ( $\text{K day}^{-1}$ )	RMSE (%)
<i>Cloudy column</i>					
1D RT	-151	230	20	38	11899
3D Emulator	72	652	8.07	12	3638
<i>Clear column</i>					
1D RT	-55	600	0.75	0.93	147
3D Emulator	-239	618	1.78	2.28	360

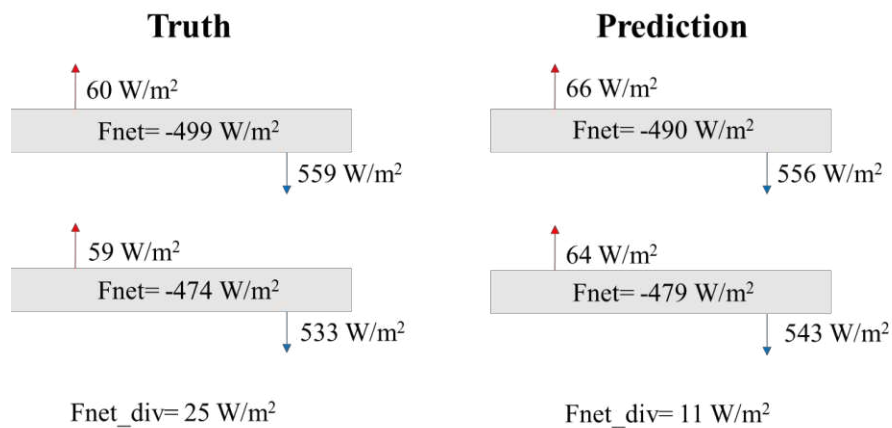


**Figure 2.14.** A diagram illustrates the link between radiative flux error and the heating rate error

### 2.4.3. *Error statistics for all grid points*

Tables 2.5 and 2.6 summarize the prediction errors from our 3D emulators for all grid points in the testing dataset. The prediction errors from 1D RT are also listed to demonstrate how much improvement the 3D emulators have made. Overall, our 3D emulator outperforms 1D RT for downwelling and upwelling fluxes in all error statistics and both solar zenith angles. The difference between our emulator and the 1D RT is larger under a more oblique solar position (i.e., SZA is 60 degrees), which the horizontal transport of radiation plays a bigger role compared to when the sun is overhead. The error distributions in our emulator for both downwelling and upwelling are symmetric to zero, meaning there is no tendency to overestimate or underestimate the predictions. The absolute error and RMSE for the downwelling predictions are larger than the upwelling predictions but smaller in the percentage error statistics for both solar positions. Since downwelling includes both direct and diffuse radiation and upwelling is only diffuse radiation, it indicates that our model has a hard time fitting the relationship between cloud field and diffuse radiation.

Our emulator does not substantially reduce the error in heating rate compared to 1D. More work is needed to improve heating rate predictions to make our emulator useful for the modeling community.

**Table 2.5.** Statistics of prediction errors from 1D RT and 3D CNN for scenes with SZA of 60°.

	Error (%)		Absolute error (%)		Absolute error (W m <sup>-2</sup> ) *(K day <sup>-1</sup> )		RMSE (W m <sup>-2</sup> ) *(K day <sup>-1</sup> )	
	1D	3D CNN	1D	3D CNN	1D	3D CNN	1D	3D CNN
Downwelling	0.76	0.24	10.30	2	41	9	80	16
Upwelling	-9	0.56	22	5	22	4	31	6
*Heating rate	198	149	483	1320	9	9	23	14

**Table 2.6.** Same as Table 2.2 but for SZA of 0°.

	Error (%)		Absolute error (%)		Absolute error (W m <sup>-2</sup> ) *(K day <sup>-1</sup> )		RMSE (W m <sup>-2</sup> ) *(K day <sup>-1</sup> )	
	1D	3D CNN	1D	3D CNN	1D	3D CNN	1D	3D CNN
Downwelling	0.74	0.08	4.06	0.80	33	7	54	12
Upwelling	2.01	0.13	37	2.53	61	3.43	109	6
*Heating rate	-396	76	885	1117	3.85	6.19	7.02	9.18

## CHAPTER 3: RETRIEVING AEROSOL OPTICAL DEPTH IN THE VICINITY OF CLOUDS USING MACHINE LEARNING TECHNIQUES

In this chapter, we introduce a new retrieval algorithm for aerosol properties in the vicinity of clouds using machine learning techniques trained by outputs of large eddy simulations in marine shallow cumulus regimes. The performance of our machine learning model will be discussed and what the machine learned will be explored using explainable AI techniques.

### 3.1. The Prototype Convolutional Neural Network

#### 3.1.1. *The training and configuration*

The goal of our machine learning model is to predict AOD over a 2.5 km x 2.5 km domain at a 100-m horizontal resolution from an input scene of reflectance values at TOA. The resolution is assigned based on the native spatial resolution of training dataset. Because of 3D effects, reflectance values directly above this domain are influenced not only by aerosol and cloud properties underneath, but also by neighboring pixels. To incorporate surrounding information for appropriate AOD predictions, the input reflectance scene size must be larger than 2.5 km x 2.5 km. Following the study of Okamura et al. (2017) for cloud retrievals, we have chosen an input scene of 4.5 km x 4.5 km, i.e., extending 1 km on all sides compared to the output domain.

To capture the complexity of the input reflectance scene, we used a Convolutional Neural Network (CNN), which is particularly useful for recognizing spatial patterns of images. Our CNN model for the retrieval method is similar to that used in 3D radiative transfer emulators. For example, we used ReLU, the same normalization method, and the Adam optimizer with the same loss function. However, they are different in the following ways. First, the CNN used here is 2D instead of 3D. Second, the size of the filters is different. Third, we only use one fully-

connected layer instead of eight layers. Finally, the input is reflectance, and the output is AOD. Details about the CNN configuration can be found in Section 2.2.

Our training and testing datasets were built from LES output. To diversify aerosol conditions and cloud morphology in our training dataset, four datasets of LES output were used and summarized in Table 1. All datasets had a domain size of 48 km x 48 km x 5 km with a horizontal resolution of 100 m and vertical resolution of 40 m. The first two datasets were generated using the forcing data collected from the Rain In Cumulus over Ocean (RICO) campaign (Raubert et al., 2007). They were taken from the same series of simulations with an initial aerosol concentration of  $200 \text{ cm}^{-3}$ , but at different output times. In contrast, Datasets 3 and 4 were generated for a much cleaner environment with an initial aerosol concentration of  $35 \text{ cm}^{-3}$ , using a forcing data that was based on ship measurements and reanalysis data over the Sulu Sea in the Philippines, (Yamaguchi et al., 2019). Additionally, Dataset 3 was generated without wind shear, while Dataset 4 was generated with wind shear. The wind-shear condition in Dataset 4 led to clouds more clustered than those in Dataset 3, as shown in Figure 3.1a–3.1d. Datasets 3 and 4 also have fewer precipitating cumulus clouds and slightly lower cloud fractions compared to Datasets 1 and 2.

**Table 3.1.** Summary of key information on LES outputs used to build the training and testing datasets. Aerosol optical depth statistics are calculated using all grid points, while liquid water paths are based on cloudy grid points, defined by the associated liquid water content exceeding or equal to  $0.01 \text{ g m}^{-3}$ .

ID	Forcing	Output time (hr)	Aerosol optical depth	Cloud fraction	Liquid water path ( $\text{g m}^{-2}$ )
1	RICO	50	$0.56 \pm 0.04$	0.26	$135 \pm 352$
2	RICO	54	$0.56 \pm 0.03$	0.20	$145 \pm 384$
3	7SEAS <sup>a</sup>	50	$0.10 \pm 0.01$	0.13	$80 \pm 172$
4	7SEAS <sup>b</sup>	50	$0.10 \pm 0.01$	0.16	$75 \pm 169$

<sup>a</sup> The environment has no wind shear.

<sup>b</sup> The environment has a vertical wind shear of  $6 \text{ m s}^{-1}$  from 0 to 6 km.

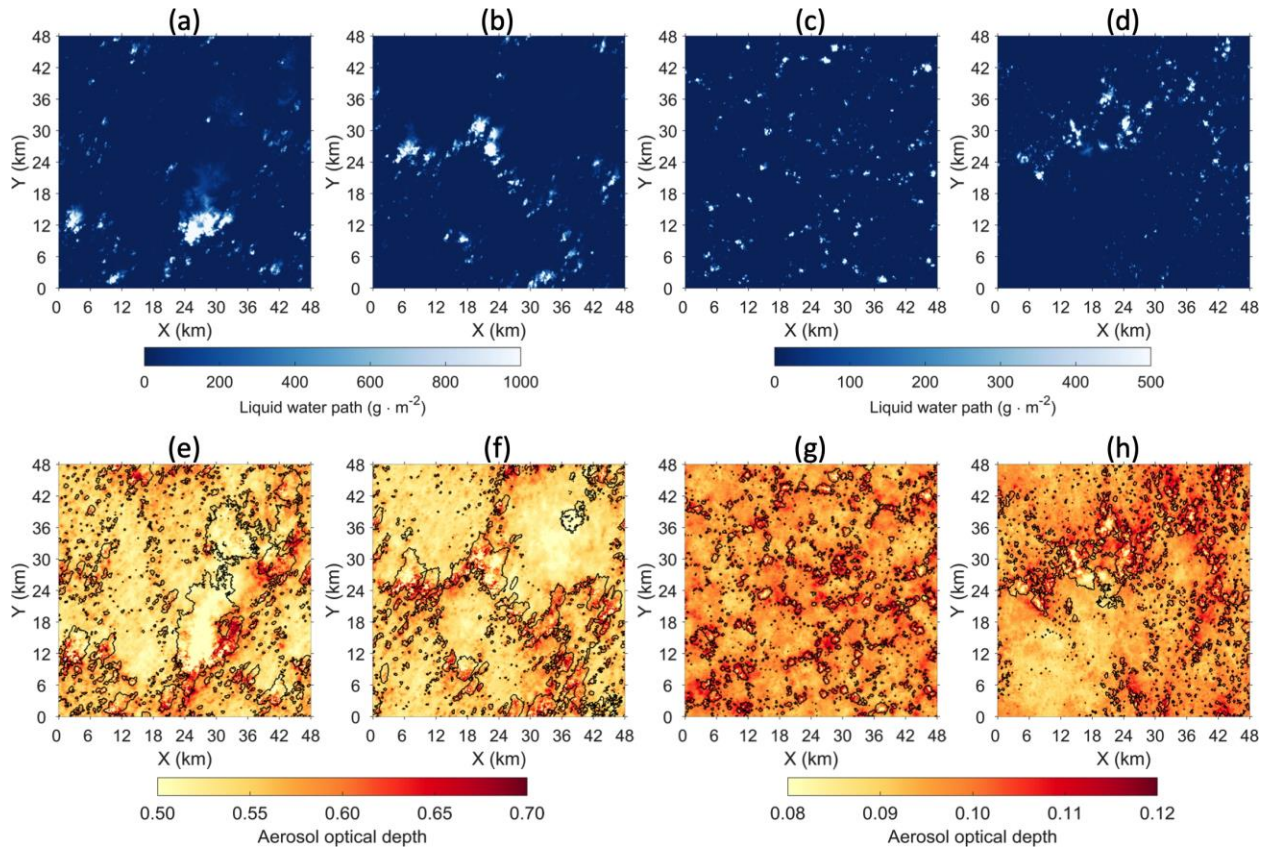


**Figure 3.1.** Snapshots of liquid water paths (a–d) and aerosol optical depths (e–h) for Datasets 1–4 (left to right, respectively). Enhanced AODs near cloud boundaries (indicated by black lines in (e)–(h)) are evident.

Cloud and aerosol optical properties in these four snapshots were calculated using the Mie theory. The aerosol type used in LES was sulfate, following a lognormal size distribution with a mean of 0.2  $\mu\text{m}$  and a geometric standard deviation of 1.5 in dry conditions. With increasing humidity near clouds, the index of refraction of aerosol particles changes and their effective radius increases due to water uptake. At a given relative humidity (RH), the index of refraction of hydrated particles is computed by (Zieger et al., 2010):

$$m_{wet} = \frac{m_{dry} + m_{water}(g^3 - 1)}{g^3} \quad (3.1)$$

where  $m_{wet}$ ,  $m_{dry}$ , and  $m_{water}$  are the index of refraction for hydrated aerosol, dry aerosol, and water, respectively.  $g$  is the diameter growth factor that describes the hygroscopic diameter growth of the particle due to water uptake with respect to its dry diameter  $D_{dry}$ , defined as:

$$g(\text{RH}) = \frac{D_{wet}(\text{RH})}{D_{dry}}. \quad (3.2)$$

For the sulfate particles used in our training dataset,  $g(\text{RH})$ , calculated from the changes in aerosol size bins in LES outputs, is shown in Figure 3.2.

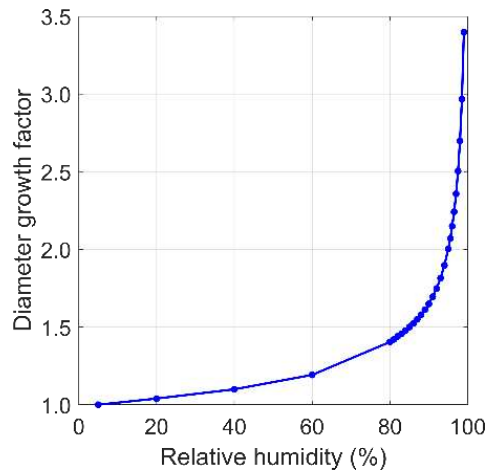


**Figure 3.2.** Diameter growth factor of sulfate particles as a function of relative humidity.

As a result, AOD is enhanced near cloud edges as shown in Figure 3.1e–3.1h. Even with these enhanced AODs near clouds, the range of the AODs from each dataset remains narrow as shown by the small standard deviations of AOD in Table 1. Hence, the distinct difference in the initial aerosol concentrations used in simulations introduces a large gap in AOD. Such a gap is not ideal for a training dataset, because the machine learning algorithm would not see any AOD values in between, which may lead to large errors in predictions. To alleviate this issue, we perturbed the aerosol mass concentration fields homogeneously everywhere by a factor ranging between 0.05–1.0 in the RICO snapshots, and by a factor ranging between 0.5–5.0 in the 7SEAS snapshots. These factor ranges were chosen to ensure that there is some AOD overlap between RICO and 7SEAS snapshots. These perturbations led to a total of 50 snapshots, 30 from RICO and 20 from 7SEAS.

From these 50 snapshots at their native resolutions, we then calculated the corresponding TOA reflectance fields at 870 nm wavelength. This wavelength was chosen to allow us to omit gas absorptions in the current setup and focus on assessing the configuration and performance of the CNN. The radiative transfer calculations were performed using the Spherical Harmonic Discrete Ordinate Method (SHDOM; Evans, 1998) under a 3D environment, assuming a solar zenith angle of  $50^\circ$ , a solar azimuth angle of  $30^\circ$ , and a viewing zenith angle of  $0^\circ$ . Rayleigh scattering were included, and ocean surface reflectance values were computed with an assumed wind speed of  $6 \text{ m s}^{-1}$ . Once the pairs of AOD and reflectance fields are ready for all 50 snapshots, we randomly sample a  $4.5 \text{ km} \times 4.5 \text{ km}$  scene to generate the training and testing datasets. This led to 0.2 M scenes, which were further split by 80% and 20% for training and testing, respectively.

### 3.1.2. The performance

Figure 3.3 shows performance of our CNN on retrieving AOD at 870 nm for one of the testing scenes. Using the retrieval uncertainty of  $(0.03 \pm 5\% \text{ AOD})$  in NASA Aerosol Robotic Network (AERONET) products (Giles et al., 2019) as the benchmark, all pixels agree to better than 0.03 with the truth. Importantly, the enhanced AODs near clouds are well predicted by the CNN. Considering the entire testing dataset, the scatter plots in Figure 3.4 indicate that 99.8% of the pixels in cloud-free regions fall within the benchmark uncertainty, and the corresponding mean error is  $\sim 0.7\%$  (as shown in Figure 3.4b). The retrieval uncertainty is estimated as  $(0.0004 \pm 4\% \text{ AOD})$ .

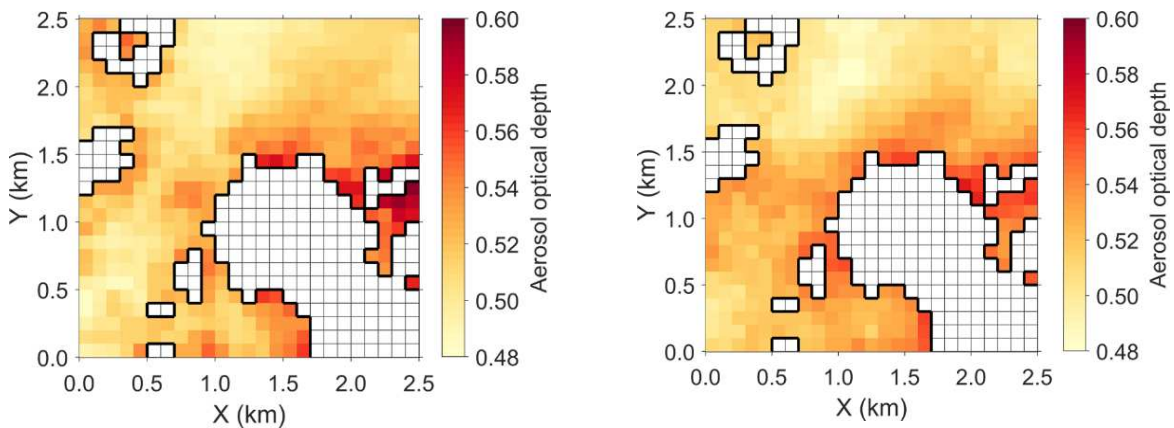


**Figure 3.3.** The performance of the CNN on a testing scene. (a) is the truth aerosol optical depth, and (b) is the prediction from the CNN. Cloudy skies are in white.

To understand the sources of information for the CNN to predict AOD near clouds, we conducted Layer-wise Relevance Propagation (LRP) analyses (Bach et al., 2015). Specifically, we used the method called  $\text{LRP}_z$  that has shown promising results regarding regression problems in geoscience (Mamalakis et al., 2021). The relevance is calculated starting from the uppermost layer in CNN and then propagated backward, layer-by-layer, to the input layer, i.e.,

$$R_i^{(l)} = \sum_{\substack{k: \text{neurons } \in (l+1) \text{ and} \\ \text{have received input from } i}} R_{i \leftarrow k}^{(l+1)}, \quad (3.3)$$

where  $R_i^{(l)}$  represents the relevance of neuron  $i$  at Layer  $l$  to the prediction of interest, and  $R_{i \leftarrow k}^{(l+1)}$  represents the relevance propagated backward from Layer  $l + 1$  to Layer  $l$ , from neuron  $k$  to neuron  $i$ . At Layer  $l + 1$ , any neuron that has received input from neuron  $i$  should be counted in calculations of  $R_i^{(l)}$ , which is indicated by the summation in equation (3.3).

Now, let us discuss how to calculate  $R_{i \leftarrow k}^{(l+1)}$  for equation (3.3). For the relevance of neuron  $k$ , we can decompose it using the contributing components from the previous layer as:

$$R_k^{(l+1)} = \sum_{\substack{i: \text{neurons } \in (l) \text{ and} \\ \text{have provided input to } k}} R_k^{(l+1)} \frac{x_i W_{ik}}{\sum_i x_i W_{ik}}, \quad (3.4)$$

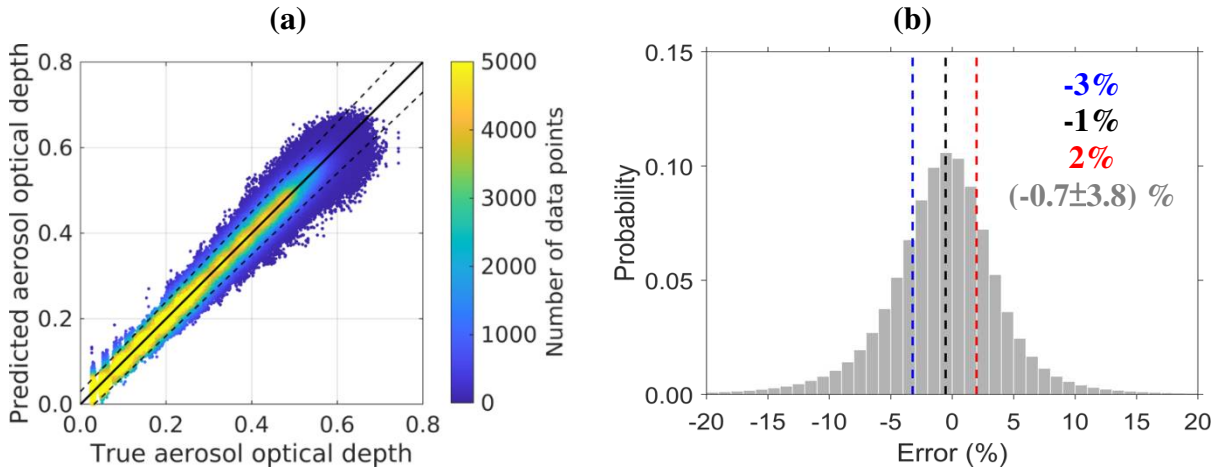


**Figure 3.4.** Plots of the predicted AOD vs. the truth for (a) all cloud-free pixels in the testing dataset, (b) is the corresponding relative error (%) distributions. The blue, black, and red dashed lines, respectively, represent the 25th, 50th, and 75th percentiles of the data. The corresponding errors for these lines are denoted in each subplot in their own color. The mean error (%)  $\pm$  the mean absolute deviation (% , using the mean as the center point) are also denoted in gray.

where  $\frac{x_i w_{ik}}{\sum_i x_i w_{ik}}$  is the relative contribution from neuron  $i$ , based on the input  $x_i$  and the weight  $w_{ik}$

between the neurons  $i$  and  $k$ . Based on the conservation of relevance, the following must hold,

$$R_k^{(l+1)} = \sum_{\substack{i: \text{neurons } \in (l) \text{ and} \\ \text{have provided input to } k}} R_{i \leftarrow k}^{(l+1)}. \quad (3.5)$$

Comparing the right-hand side of equation (3.4) and (3.5), we then get

$$R_{i \leftarrow k}^{(l+1)} = R_k^{(l+1)} \frac{x_i w_{ik}}{\sum_i x_i w_{ik}}, \quad (3.6)$$

where the neuron  $i$  belongs to Layer  $l$  and has provided input to the neuron  $k$ . In short, the relevance can be thought as the local contribution to the prediction. Since ReLU has been used as the activation function, the attribution from LRPz is equivalent to the product of input pixel value and the gradient of the CNN at the input pixel. The sign of the relevance is positive if the local contribution of the neuron has the same sign as the sum of the contribution from all input neurons. In contrast, the sign of the relevance is negative if the signs of the local contribution and the aggregated contribution are different.

Figure 3.5 shows some examples of the relevance heat maps for a selected testing scene. For convenience, the input reflectance field for the scene is also shown to relate the pixels of interest to cloud locations. A few findings are noted here.

- For all example pixels, relevance from Cloud A and B is evident no matter whether the pixel of interest is relatively far from clouds or near clouds. Considering that the optical influence of clouds is beyond their physical boundaries and can enhance cloud-free sky pixels as far as 5 km (Várnai and Marshak, 2011), which is comparable with our input

domain dimension, this relevance result is reasonable and matches our understanding of 3D radiative transfer.

- Figures 3.5b and 3.5c show that the relative relevance of Cloud A and B vary depending on the location of pixel of interest. When the pixel of interest moves from the left to the right, the relevance of Cloud B fades away and the relevance of Cloud A becomes stronger. The relevance of Cloud B remains weak for all other pixels that are further away.
- For pixels that are relatively far from clouds (Figures 3.5d and 3.5f), we see strong influence surrounding the pixel of interest with a negative sign. Recall that the negative sign indicates that the contribution has a different sign from that of the aggregated contribution. Since pixels far from clouds typically have the lowest AOD and reflectance compared to other areas that are influenced by humidity and clouds, the local contribution needs to lower AOD to match what has been observed in the training dataset. The strong negative local relevance fades away when moving the pixel of interest toward clouds, since the influence from cloudy pixels becomes more significant.

Although results from LRPz analyses generally match our understanding of radiative transfer, the relatively small contributions in clear-sky pixels to AOD retrievals at near-cloud pixels are a concern. As explained above, the attribution from LRPz can largely depend on the input pixel value; hence, the generally small contributions from clear-sky pixels can be the consequence of the LRPz technique itself, and the role of near-cloud reflectance remains unclear. Based on the large contributions from cloudy pixels shown in LRPz results, we propose two hypotheses to explain how our CNN predicts AOD. The first hypothesis is that the CNN identifies cloud locations, retrieves AOD for pixels far away from clouds, and then interpolates AOD based on the relationships between AOD and distances to nearest clouds. In this

hypothesis, the CNN does not need to actively account for 3D radiative effects in observed reflectance values and hence the contributions of pixels in the transition zone are minimum. The second hypothesis is that the CNN does actively correct the 3D radiative effects in observed reflectances and uses the corrected reflectance field to retrieve AOD. To test which hypothesis is correct, we conducted an experiment as explained below.

Using the scene shown in Fig. 3.3, we applied the same input reflectance field, except reflectance in cloud-free regions to a constant that corresponds to the reflectance with a background AOD of 0.49 (Fig. 3.6a). If the first hypothesis is correct, i.e., the CNN only minds the cloud locations and the background reflectance value, then the retrieved AOD field will still show the enhancement near clouds, even though there is no enhancement in the input reflectance field. Such false AOD enhancement should be found all around the clouds, no matter whether pixels are located on the illuminated or shadowing side. However, if the second hypothesis is correct, i.e., the CNN actively accounts for 3D radiative effects, then the CNN will tend to make a larger reflectance correction in near-cloud regions than in regions far from clouds. As a result, the trend of AOD versus distance to nearest clouds should disappear or even reverse. Additionally, since the reflectance on the shadow side is supposed to be lower than the illuminated side at a given AOD, the CNN will need to account for the shadowing effect during the prediction process. Hence, if the CNN indeed recognizes the sun-viewing geometry, then our manipulated constant reflectance field will lead to a higher AOD on the shadowing side than the illuminated side given the same reflectance on both sides.

Figure 3.6b shows the retrieved AOD field from the manipulated reflectance input. The retrievals show no evidence of AOD enhancement. Instead, the retrievals on the shadowing side are ~15% larger than those on the illuminated side. These findings suggest that the second

hypothesis is much more plausible. Hence, our CNN likely actively accounts for 3D cloud radiative effects and correct them in the input reflectance for predicting AOD. In short, it is not surprising that the LRPz technique made a large attribution to cloudy pixels in AOD predictions, since the largest contribution in reflectance enhancement comes from clouds (Várnai and Marshak, 2011). However, cautions should be exercised in interpreting the small attributions in clear-sky regions. Our test suggests that the reflectances in the transition zone remain important for the CNN to retrieve AOD after accounting for 3D cloud radiative effects.

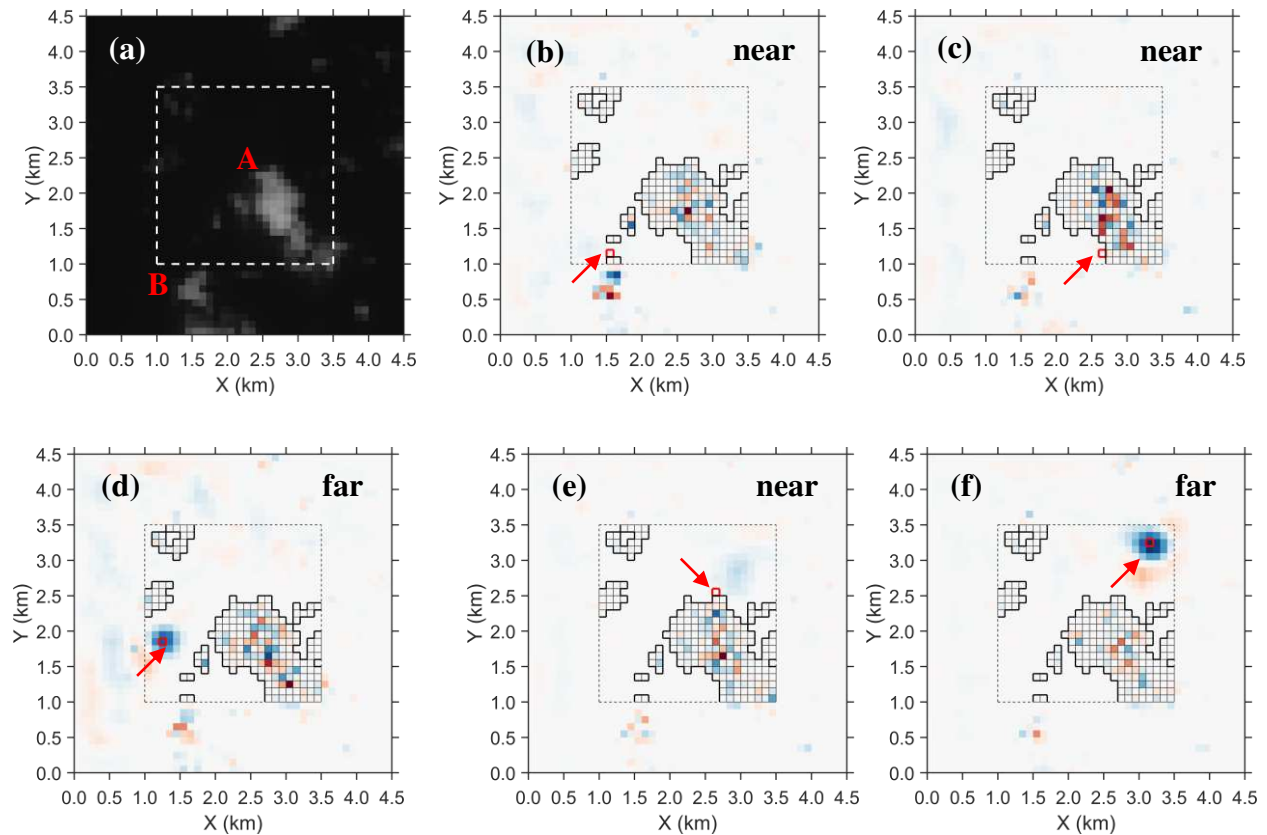


**Figure 3.5.** (a) Input reflectance field for the testing scene used in Figure 3.2. (b)–(i) the corresponding heat maps of relevance based on our prototype CNN for selected pixels. The pixels of interest are marked using red boxes and pointed out by the red arrows. Note that each heat map has been normalized by the corresponding maximum absolute relevance within each map, making the range to always fall between -1 (blue) to 1 (red).

(a)

(b)

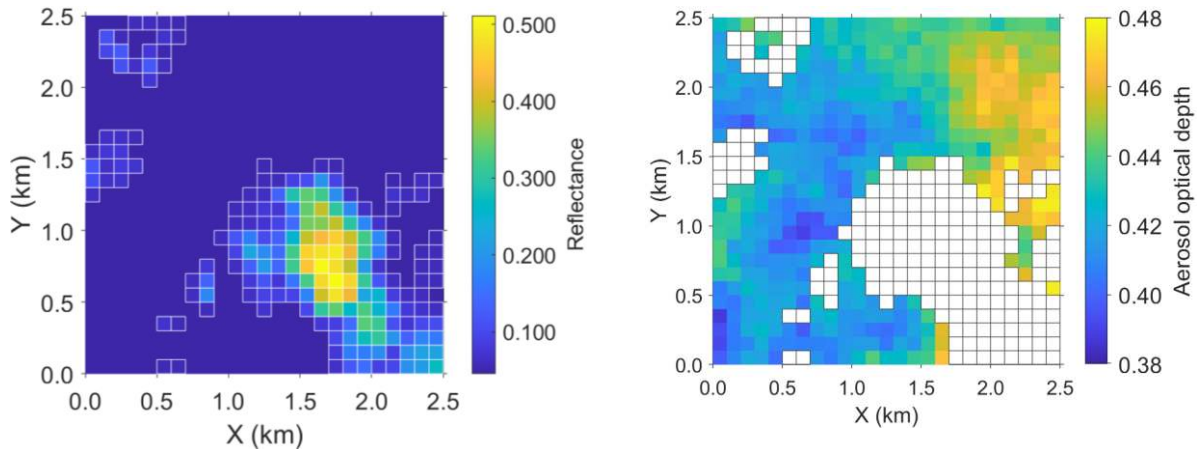


**Figure 3.6.** (a) An input reflectance field for the CNN to predict AOD. The scene is same as Fig. 3.3., but with a fixed reflectance value in cloud-free regions. (b) The corresponding AOD predictions. Gridded pixels indicate the presence of clouds.

### 3.2. A case study using MODIS observations

In this section, we apply our CNN approach to an Aqua satellite overpass near Bermuda at ~17:25 UTC on 22 October 2010 and compare our predicted AOD to the MODIS operational Level 2 Collection 6 aerosol products. We selected a ~20-km wide and ~500-km long scene that is over ocean, away from sun-glint, and composed of scattered shallow cumuli (see Figure 3.7a) that could be challenging for the MODIS operational algorithm to retrieve AOD. The range of solar zenith angles is between  $47^\circ$  to  $51^\circ$ , and the solar azimuth angle is  $\sim 210^\circ$  clockwise from the north. The viewing zenith angle is within  $1^\circ$  from the nadir.

The operational product (MYD04\_3K) has a horizontal resolution of 3 km with retrieval uncertainty of  $0.03 \pm 5\%$  AOD. For pixels over ocean, the retrieval is based on the Dark Target algorithm (Tanré et al., 1997; Remer et al., 2005, 2013; Levy et al., 2013). In their algorithm, 500-m resolution pixels influenced by clouds or ocean sediments are discarded, and then 25% of the darkest and 25% of the brightest pixels in a 3 km x 3 km domain are also discarded. After this screening, reflectances over the remaining pixels are averaged and then compared to pre-calculated lookup tables to find the best matched AOD. The lookup tables used in the Dark

Target algorithm were built using pre-defined fine-mode and coarse-mode aerosol models in various ocean wind conditions. If the remaining pixels in a 3 km x 3 km domain are fewer than 5, the algorithm will not be performed, and a missing retrieval will be reported. For the selected scene, 50% of the areas lack AOD retrievals due to being near clouds or in clouds, as shown in Figure 3.7b.

To retrieve AOD, we regenerated our training dataset and retrain the CNN because the sun-viewing geometry of this scene is different from the proof-of-concept case in Section 3.1. As a result, we built 49 sets of training datasets and the corresponding CNNs to cover the variation of SZA, using the same LES outputs but with the following changes. First, we use MODIS pre-defined aerosol models to minimize the comparison discrepancy introduced by the difference in aerosol models, since we aim to investigate whether our predictions agree with MODIS retrievals in clear-sky regions far from clouds. For the selected scene, most MODIS retrievals suggest that the dominant fine mode is wet water-soluble particles, and the dominant coarse mode is sea salt. The fine mode fraction varies from 0.3 to 0.7. For simplicity, we used a fine mode fraction of 0.5 when rebuilding our training dataset. Second, the diameter growth factor of the wet water-soluble particles as a function of humidity is set to be same as that used in the proof-of-concept case. But for sea salt, the growth factor function is taken from Zieger et al. (2017). Based on their growth factors, the refractive index is calculated based on a volume weighting between aerosol particles and water, as shown in Zeiger et al. (2010). Finally, we assigned a wind speed of 6 m s<sup>-1</sup> in calculations of ocean surface reflectance, based on the 3-Hourly NCEP North American Regional Reanalysis (NARR) Composites.

As shown in Figures 3.7b and 3.7c, our CNNs predict a similar spatial pattern to the MODIS product throughout the scene. To perform comparisons, we aggregate our CNN

predictions from 500 m to 3 km. In the clear-sky regions (e.g., 60–120 km along the track), the AOD difference between two retrieval sets is generally within MODIS retrieval uncertainty (Figure 3.7d). Considering that these two methods are based on different radiative transfer calculations (3D vs 1D), and that some pixels are based on different aerosol models and fine mode fractions, the agreement within the expected MODIS retrieval uncertainty in the clear-sky regions suggest that our CNNs work well. Near clouds, the AOD difference between two is generally within the MODIS retrieval uncertainty; only a few pixels are associated with larger difference.

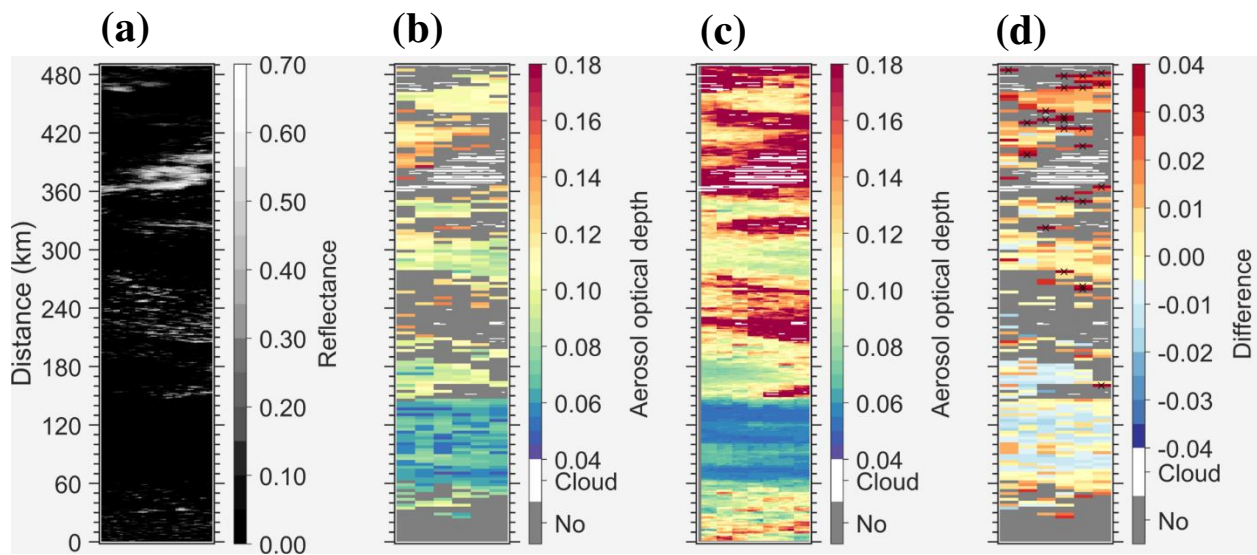


**Figure 3.7.** (a) Reflectance at 857 nm wavelength observed from MODIS onboard the Aqua Satellite at 17:25 UTC on 22 October 2010. (b) and (c) are the corresponding AOD retrievals at 857 nm from the MODIS operational product and our CNN, respectively. The AOD difference in (d) is calculated by subtracting MODIS retrievals from CNN retrievals that are averaged to 3 km resolution. White areas in (b) and (d) represent the regions in which the AOD cannot be retrieved by the dark target algorithm. Note that (a) and (c) are plotted with a pixel resolution of 500 m, while (b) and (d) are with pixel resolution of 3 km. The regions marked with crosses in (d) indicate the difference between the CNN retrievals and the MODIS retrievals exceed the MODIS retrieval uncertainty.

## CHAPTER 4: SUMMARY AND FUTURE WORK

### 4.1. Summary

This thesis set out to tackle an outstanding issue in aerosol remote sensing, namely the lack of observations of aerosol properties near clouds due to 3D radiative effects. The optical and microphysical properties of aerosols near clouds are distinctly different from those far from clouds. Neglecting near-cloud aerosols is not only a missed opportunity to have a rich dataset for understanding aerosol-cloud interactions, but may also have a significant impact on existing estimates of aerosol radiative forcing.

Capitalizing on recent advance in machine learning techniques, we have developed 3D shortwave radiative transfer emulators that are fast and accurate and can be used in existing retrieval methods for aerosols or in models for predicting fluxes. The emulators are built based on 3D Convolutional Neural Network (CNN). They require input of 1D atmospheric profiles and 3D cloud water content and cloud effective radius over a 7.5 km x 7.5 km x 4.5 km domain, and provide flux predictions in a 0.5 km x 0.5 km x 4.5 km domain. To address questions listed in Section 1.2.1, our key findings are summarized below:

- *How well do 3D SW RT emulators capture the spatial distribution of surface radiation for highly inhomogeneous cumulus regime?*

We have trained our emulators using scenes with shallow cumuli. For such highly inhomogeneous clouds, the emulators well predict the spatial patterns and the PDF of surface downwelling fluxes – the errors in domain average flux for SZA of 60° and for overhead sun were negligible and  $1\text{W m}^{-2}$  (less than 0.1%), respectively.

- *What are the errors in predictions of flux and heating rate? How are these errors compared to those from 1D RT calculations?*

The root-mean-square-error for flux and heating rate predictions were  $16 \text{ W m}^{-2}$  for downwelling,  $6 \text{ W m}^{-2}$  for upwelling, and  $14 \text{ K day}^{-1}$  for heating rate. The performance of CNN predictions is found to be consistent across all the scene regardless cloudiness, although the prediction tends to be noisy when the heating rate is small. Compared to 1D RT calculations, 3D emulators reduced the errors in flux and heating rate by a factor of 4 and 1.5, respectively.

We have also applied CNN to develop a new method for retrieving AOD without the need of cloud screening or corrections of 3D radiative effect. This method requires input of 2D fields of reflectance measurements over a  $4.5 \text{ km} \times 4.5 \text{ km}$  domain and provides AOD retrievals over a  $2.5 \text{ km} \times 2.5 \text{ km}$  domain. The finest resolution that the method can accommodate is 100 m. To address questions listed in Section 1.2.2, key findings are summarized below:

- *How well does the machine-learning based method retrieve aerosol optical depth, particularly in the vicinity of clouds?*

The retrieval uncertainty is  $(0.0004 \pm 4\% \text{ AOD})$  for cloud-free areas, including the vicinity of clouds. Based on our designed experiment, we have found that the AOD is retrieved by accounting for 3D cloud radiative effects in reflectance measurements, rather than by a simple inversion. The performance of the CNN also appears consistent regardless of pixels being on the illuminated or showing side.

- *Are results from explainable AI techniques for near-cloud AOD predictions supported by our understanding of radiative transfer?*

To understand what information the CNN has largely relied on for retrieving near-cloud AOD, we have conducted Layer-wise Relevance Propagation analyses. The first striking finding is that cloudy pixels have large influence in AOD retrievals for all pixels in the 2.5 km x 2.5 km scene. This is consistent with the expectations from radiative transfer since cloud's influence can extend at least 5 km away from its boundary. We have also found that AOD retrievals near clouds are highly relevant to cloudy pixels, not the background cloud-free pixels. This is encouraging because the relevance may have implications in future studies in aerosol-cloud interactions.

- *How well does the machine-learning based method perform in real world applications, compared to existing operational products?*

We applied our retrieval method to MODIS observations over oceans. Since current operational products work best over dark oceans for pixels far from clouds, we use their AOD retrievals taken from that specific condition as reference for evaluations. Results from a case study demonstrate that the agreement for pixels far from clouds is generally within 0.03, the retrieval uncertainty of our CNN.

## 4.2. Future work

In Chapter 2, we explored the feasibility of using machine learning techniques to build the 3D shortwave radiative transfer emulator. While the emulators nicely replicated the 3D radiative effects of clouds, more work is needed to generalize this framework.

The generalization includes extensions in cloud type, background aerosol properties, sun-viewing geometry, and surface reflectance treatment. The emulators are currently designed for low clouds. To build emulators for mixed-phase clouds or ice clouds, the input domain size needs to be sufficiently large to capture the paths of direct beam, since these types of clouds tend to develop to or locate at higher altitudes. Additionally, establishing a representative training dataset for these cloud types can be challenging. Observations for mixed-phase clouds mainly rely on ground-based radar measurements, which have large uncertainty, especially in ice number concentration and particle size that are crucial for determining shortwave radiation. One can build the training dataset from model output (similar to our current approach), but needs to recognize that many ice processes such as ice number production and riming remain highly uncertain in ice microphysics schemes.

Compared to extension to different cloud types, extensions regarding aerosols and sun-viewing geometry are more straightforward to handle. In CNN, aerosol properties may be able to input in the manner similar to gases. For sun-viewing geometry, one can build emulators for various viewing angles, and solar zenith and azimuth angles, and then interpolate output to any given combination of sun-view geometry. An alternative approach is to allow CNN to learn the sun-viewing dependence directly.

The difficulty of surface reflectance treatment depends on applications. For model applications, the assignment of shortwave surface reflectance typically follows fixed values or

simple empirical relationships. The emulators can be built using the same assignment for consistency. For remote sensing applications, it may be best to incorporate surface reflectance models directly to allow CNN to calculate the corresponding surface reflectance given the input parameters, e.g., wind speed and chlorophyll-a concentration for ocean albedo.

In this thesis, we present one of possible CNN configurations for predicting 3D radiation predictions. Currently, the ratio of the number of trainable parameters in the CNN to the number of training samples is large and may not be necessary. The large errors in heating rate also warrant improvement in the current CNN. We will systematically reduce the number of the fully connected layers to identify the least complex network that has similar performance to the current CNN. We will also implement regularization techniques (e.g., batch normalization or dropout) and apply physical constraints by making heating rate in the cost function of the network to improve predictions of heating rate.

Similar to the 3D emulators, the aerosol retrieval method presented in Chapter 3 is also designed only for warm clouds, certain aerosol models and single wavelength. Since spectral information provides critical information on aerosol type and particle size, we plan to extend the work to the wavelengths ranging from 440 nm to 1640 nm. Unlike most existing retrieval methods that have several aerosol models and find the best-fit mixture of fine and coarse modes, our CNN needs to pre-specify aerosol models for training. To meet operational retrieval purposes, the CNN needs to incorporate mixtures of fine and coarse aerosols, ideally, similar to the database used for the multi-angle imaging spectroradiometer (MISR) operational algorithm (Kahn and Gaitley, 2015). Extensive analyses will be needed to understand how the CNN handle a variety of mixtures.

Following the case study shown in Section 3.2, aerosol direct radiative effects of the transition zone in the SW spectral region can be calculated to quantify its relative importance compared to the current estimates. Although not all aerosol types have significant hygroscopic growth as sea salt, we expect that incorporating hydrated aerosols will lead to a more negative value in radiative forcing estimate, and the relative contributions of various aerosol types to the total forcing may change once hydration effects are included.

## REFERENCES

- Agarap, A. F. (2018). Deep learning using rectified linear units (relu). arXiv preprint arXiv:1803.08375.
- Bach, S., Binder, A., Montavon, G., Klauschen, F., Müller, K. R., & Samek, W. (2015). On pixel-wise explanations for non-linear classifier decisions by layer-wise relevance propagation. *PloS one*, 10(7), e0130140.
- Belochitski, A., Binev, P., DeVore, R., Fox-Rabinovitz, M., Krasnopolsky, V., & Lamby, P. (2011). Tree approximation of the long wave radiation parameterization in the NCAR CAM global climate model. *Journal of Computational and Applied Mathematics*, 236(4), 447-460.
- Benner, T. C., & Evans, K. F. (2001). Three-dimensional solar radiative transfer in small tropical cumulus fields derived from high-resolution imagery. *Journal of Geophysical Research: Atmospheres*, 106(D14), 14975-14984.
- Board, S. S., & National Academies of Sciences, Engineering, and Medicine. (2019). *Thriving on our changing planet: A decadal strategy for Earth observation from space*. National Academies Press.
- Cahalan, R. F., Ridgway, W., Wiscombe, W. J., Bell, T. L., & Snider, J. B. (1994). The albedo of fractal stratocumulus clouds. *Journal of Atmospheric sciences*, 51(16), 2434-2455.

- Charlson, R. J., Ackerman, A. S., Bender, F. A. M., Anderson, T. L., & Liu, Z. (2007). On the climate forcing consequences of the albedo continuum between cloudy and clear air. *Tellus B: Chemical and Physical Meteorology*, 59(4), 715-727.
- Chevallier, F., Chéruy, F., Scott, N. A., & Chédin, A. (1998). A neural network approach for a fast and accurate computation of a longwave radiative budget. *Journal of applied meteorology*, 37(11), 1385-1397.
- Chevallier, F., Chédin, A., Chéruy, F., & Morcrette, J. J. (2000). TIGR-like atmospheric-profile databases for accurate radiative-flux computation. *Quarterly Journal of the Royal Meteorological Society*, 126(563), 777-785.
- Drueke, S., Kirshbaum, D. J., & Kollias, P. (2020). Environmental sensitivities of shallow-cumulus dilution—Part 1: Selected thermodynamic conditions. *Atmospheric Chemistry and Physics*, 20(21), 13217-13239.
- Eck, T. F., Holben, B. N., Reid, J. S., Arola, A., Ferrare, R. A., Hostetler, C. A., ... & Sinyuk, A. (2014). Observations of rapid aerosol optical depth enhancements in the vicinity of polluted cumulus clouds. *Atmospheric Chemistry and Physics*, 14(21), 11633-11656.
- Evans, K. F. (1998). The spherical harmonics discrete ordinate method for three-dimensional atmospheric radiative transfer. *Journal of the Atmospheric Sciences*, 55(3), 429-446.
- Eytan, E., Koren, I., Altaratz, O., Kostinski, A. B., & Ronen, A. (2020). Longwave radiative effect of the cloud twilight zone. *Nature Geoscience*, 13(10), 669-673.

- Forster, P., Storelvmo, T., Armour, K., Collins, W., Dufresne, J. L., Frame, D., ... & Zhang, H. (2021). The Earth's Energy Budget, Climate Feedbacks, and Climate Sensitivity. *Climate Change*.
- Fu, Q., & Liou, K. N. (1992). On the correlated k-distribution method for radiative transfer in nonhomogeneous atmospheres. *Journal of Atmospheric Sciences*, 49(22), 2139-2156.
- Gabriel, P. M., & Evans, K. F. (1996). Simple radiative transfer methods for calculating domain-averaged solar fluxes in inhomogeneous clouds. *Journal of Atmospheric Sciences*, 53(6), 858-877.
- Giles, D. M., Sinyuk, A., Sorokin, M. G., Schafer, J. S., Smirnov, A., Slutsker, I., ... & Lyapustin, A. I. (2019). Advancements in the Aerosol Robotic Network (AERONET) Version 3 database—automated near-real-time quality control algorithm with improved cloud screening for Sun photometer aerosol optical depth (AOD) measurements. *Atmospheric Measurement Techniques*, 12(1), 169-209.
- Gristey, J. J., Feingold, G., Glenn, I. B., Schmidt, K. S., & Chen, H. (2020). On the relationship between shallow cumulus cloud field properties and surface solar irradiance. *Geophysical Research Letters*, 47(22), e2020GL090152.
- Gounou, A., & Hogan, R. J. (2007). A sensitivity study of the effect of horizontal photon transport on the radiative forcing of contrails. *Journal of the atmospheric sciences*, 64(5), 1706-1716.
- Gustafson Jr, W. I., Vogelmann, A. M., Li, Z., Cheng, X., Dumas, K. K., Endo, S., ... & Xiao, H. (2020). The large-eddy simulation (LES) atmospheric radiation measurement (ARM)

symbiotic simulation and observation (LASSO) activity for continental shallow convection. *Bulletin of the American Meteorological Society*, 101(4), E462-E479.

Hogan, R. J., & Shonk, J. K. (2013). Incorporating the effects of 3D radiative transfer in the presence of clouds into two-stream multilayer radiation schemes. *Journal of the atmospheric sciences*, 70(2), 708-724.

Jahani, B., Andersen, H., Calbó, J., González, J. A., & Cermak, J. (2021). Longwave Radiative Effect of the Cloud-Aerosol Transition Zone Based on CERES Observations. *Atmospheric Chemistry and Physics Discussions*, 1-17.

Jakub, F., & Mayer, B. (2015). A three-dimensional parallel radiative transfer model for atmospheric heating rates for use in cloud resolving models—The TenStream solver. *Journal of Quantitative Spectroscopy and Radiative Transfer*, 163, 63-71.

Kahn, R. A., & Gaitley, B. J. (2015). An analysis of global aerosol type as retrieved by MISR. *Journal of Geophysical Research: Atmospheres*, 120(9), 4248-4281.

Kassianov, E., Ovchinnikov, M., Berg, L. K., McFarlane, S. A., & Flynn, C. (2009). Retrieval of aerosol optical depth in vicinity of broken clouds from reflectance ratios: Sensitivity study. *Journal of Quantitative Spectroscopy and Radiative Transfer*, 110(14-16), 1677-1689.

Kim, B. G., Schwartz, S. E., Miller, M. A., & Min, Q. (2003). Effective radius of cloud droplets by ground-based remote sensing: Relationship to aerosol. *Journal of Geophysical Research: Atmospheres*, 108(D23).

- Krasnopolsky, V. M., Fox-Rabinovitz, M. S., & Chalikov, D. V. (2005). New approach to calculation of atmospheric model physics: Accurate and fast neural network emulation of longwave radiation in a climate model. *Monthly Weather Review*, 133(5), 1370-1383.
- Krasnopolsky, V. M., & Fox-Rabinovitz, M. S. (2006). Complex hybrid models combining deterministic and machine learning components for numerical climate modeling and weather prediction. *Neural Networks*, 19(2), 122-134.
- Krasnopolsky, V. M., Fox-Rabinovitz, M. S., Hou, Y. T., Lord, S. J., & Belochitski, A. A. (2010). Accurate and fast neural network emulations of model radiation for the NCEP coupled climate forecast system: climate simulations and seasonal predictions. *Monthly Weather Review*, 138(5), 1822-1842.
- Konwar, M., Panicker, A. S., Axisa, D., & Prabha, T. V. (2015). Near-cloud aerosols in monsoon environment and its impact on radiative forcing. *Journal of Geophysical Research: Atmospheres*, 120(4), 1445-1457.
- Koren, I., Remer, L. A., Kaufman, Y. J., Rudich, Y., & Martins, J. V. (2007). On the twilight zone between clouds and aerosols. *Geophysical research letters*, 34(8).
- Levy, R. C., Mattoo, S., Munchak, L. A., Remer, L. A., Sayer, A. M., Patadia, F., & Hsu, N. C. (2013). The Collection 6 MODIS aerosol products over land and ocean. *Atmospheric Measurement Techniques*, 6(11), 2989-3034.
- Lim, K. S. S., Riihimaki, L., Comstock, J. M., Schmid, B., Sivaraman, C., Shi, Y., & McFarquhar, G. M. (2016). Evaluation of long-term surface-retrieved cloud droplet

- number concentration with in situ aircraft observations. *Journal of Geophysical Research: Atmospheres*, 121(5), 2318-2331.
- Mamalakis, A., Ebert-Uphoff, I., & Barnes, E. A. (2021). Neural Network Attribution Methods for Problems in Geoscience: A Novel Synthetic Benchmark Dataset. arXiv preprint arXiv:2103.10005.
- Marshak, A., Davis, A., Wiscombe, W., & Cahalan, R. (1995). Radiative smoothing in fractal clouds. *Journal of Geophysical Research: Atmospheres*, 100(D12), 26247-26261.
- Marshak, A., Davis, A., Cahalan, R. F., & Wiscombe, W. (1998). Nonlocal independent pixel approximation: Direct and inverse problems. *IEEE Transactions on Geoscience and Remote Sensing*, 36(1), 192-205.
- Mlawer, E. J., Taubman, S. J., Brown, P. D., Iacono, M. J., & Clough, S. A. (1997). Radiative transfer for inhomogeneous atmospheres: RRTM, a validated correlated-k model for the longwave. *Journal of Geophysical Research: Atmospheres*, 102(D14), 16663-16682.
- National Academies of Sciences, Engineering, and Medicine. (2018). National Academies of Sciences—Engineering and Medicine. Thriving on Our Changing Planet: A Decadal Strategy for Earth Observation from Space; The National Academies Press: Washington, DC, USA, 716.
- Okamura, R., Iwabuchi, H., & Schmidt, K. S. (2017). Feasibility study of multi-pixel retrieval of optical thickness and droplet effective radius of inhomogeneous clouds using deep learning. *Atmospheric Measurement Techniques*, 10(12), 4747-4759.

- Pal, A., Mahajan, S., & Norman, M. R. (2019). Using deep neural networks as cost-effective surrogate models for super-parameterized E3SM radiative transfer. *Geophysical Research Letters*, 46(11), 6069-6079.
- Pincus, R., Hannay, C., & Evans, K. F. (2005). The accuracy of determining three-dimensional radiative transfer effects in cumulus clouds using ground-based profiling instruments. *Journal of the atmospheric sciences*, 62(7), 2284-2293.
- Rauber, R. M., Stevens, B., Ochs III, H. T., Knight, C., Albrecht, B. A., Blyth, A. M., ... & Zuidema, P. (2007). Rain in shallow cumulus over the ocean: The RICO campaign. *Bulletin of the American Meteorological Society*, 88(12), 1912-1928.
- Reichstein, M., Camps-Valls, G., Stevens, B., Jung, M., Denzler, J., & Carvalhais, N. (2019). Deep learning and process understanding for data-driven Earth system science. *Nature*, 566(7743), 195-204.
- Remer, L. A., Kaufman, Y. J., Tanré, D., Mattoo, S., Chu, D. A., Martins, J. V., ... & Holben, B. N. (2005). The MODIS aerosol algorithm, products, and validation. *Journal of atmospheric sciences*, 62(4), 947-973.
- Remer, L. A., Mattoo, S., Levy, R. C., & Munchak, L. A. (2013). MODIS 3 km aerosol product: algorithm and global perspective. *Atmospheric Measurement Techniques*, 6(7), 1829-1844.
- Roh, S., & Song, H. J. (2020). Evaluation of neural network emulations for radiation parameterization in cloud resolving model. *Geophysical Research Letters*, 47(21), e2020GL089444.

- Sengupta, M., Clothiaux, E. E., Ackerman, T. P., Kato, S., & Min, Q. (2003). Importance of accurate liquid water path for estimation of solar radiation in warm boundary layer clouds: An observational study. *Journal of climate*, 16(18), 2997-3009.
- Spencer, R. S., Levy, R. C., Remer, L. A., Mattoo, S., Arnold, G. T., Hlavka, D. L., ... & Platnick, S. E. (2019). Exploring aerosols near clouds with high-spatial-resolution aircraft remote sensing during SEAC4RS. *Journal of Geophysical Research: Atmospheres*, 124(4), 2148-2173.
- Stap, F. A., Hasekamp, O. P., Emde, C., & Röckmann, T. (2016). Multiangle photopolarimetric aerosol retrievals in the vicinity of clouds: Synthetic study based on a large eddy simulation. *Journal of Geophysical Research: Atmospheres*, 121(21), 12-914.
- Tackett, J. L., & Di Girolamo, L. (2009). Enhanced aerosol backscatter adjacent to tropical trade wind clouds revealed by satellite-based lidar. *Geophysical Research Letters*, 36(14).
- Tanré, D., Kaufman, Y. J., Herman, M., & Mattoo, S. (1997). Remote sensing of aerosol properties over oceans using the MODIS/EOS spectral radiances. *Journal of Geophysical Research: Atmospheres*, 102(D14), 16971-16988.
- Twohy, C. H., Clement, C. F., Gandrud, B. W., Weinheimer, A. J., Campos, T. L., Baumgardner, D., ... & Tan, D. (2002). Deep convection as a source of new particles in the midlatitude upper troposphere. *Journal of Geophysical Research: Atmospheres*, 107(D21), AAC-6.

- Twohy, C. H., Coakley Jr, J. A., & Tahnk, W. R. (2009). Effect of changes in relative humidity on aerosol scattering near clouds. *Journal of Geophysical Research: Atmospheres*, 114(D5).
- Várnai, T., & Davies, R. (1999). Effects of cloud heterogeneities on shortwave radiation: Comparison of cloud-top variability and internal heterogeneity. *Journal of the atmospheric sciences*, 56(24), 4206-4224.
- Várnai, T., & Marshak, A. (2009). MODIS observations of enhanced clear sky reflectance near clouds. *Geophysical Research Letters*, 36(6).
- Várnai, T., & Marshak, A. (2010). Global CALIPSO observations of aerosol changes near clouds. *IEEE Geoscience and Remote Sensing Letters*, 8(1), 19-23.
- Várnai, T., & Marshak, A. (2014). Near-cloud aerosol properties from the 1 km resolution MODIS ocean product. *Journal of Geophysical Research: Atmospheres*, 119(3), 1546-1554.
- Várnai, T., Marshak, A., & Eck, T. F. (2017). Observation-based study on aerosol optical depth and particle size in partly cloudy regions. *Journal of Geophysical Research: Atmospheres*, 122(18), 10-013.
- Vogelmann, A. M., McFarquhar, G. M., Ogren, J. A., Turner, D. D., Comstock, J. M., Feingold, G., ... & Toto, T. (2012). RACORO extended-term aircraft observations of boundary layer clouds. *Bulletin of the American Meteorological Society*, 93(6), 861-878.
- Wapler, K., and B. Mayer, 2008: A fast three-dimensional approximation for the

calculation of surface irradiance in large-eddy simulation models. *J. Appl. Meteor. Climatol.*, 47, 3061–3071.

Weather Research and Forecasting (WRF) Model (Skamarock et al., 2008) or the System for Atmospheric Modeling (SAM) (Khairoutdinov and Randall, 2003).

Wen, G., Marshak, A., Levy, R. C., Remer, L. A., Loeb, N. G., Várnai, T., & Cahalan, R. F. (2013). Improvement of MODIS aerosol retrievals near clouds. *Journal of Geophysical Research: Atmospheres*, 118(16), 9168-9181.

Wen, G., Marshak, A., Várnai, T., & Levy, R. (2016). Testing the two-layer model for correcting near-cloud reflectance enhancement using LES/SHDOM-simulated radiances. *Journal of Geophysical Research: Atmospheres*, 121(16), 9661-9674.

Wissmeier, U., Buras, R., & Mayer, B. (2013). paNTICA: A fast 3D radiative transfer scheme to calculate surface solar irradiance for NWP and LES models. *Journal of applied meteorology and climatology*, 52(8), 1698-1715.

Wu, X., Balmes, K. A., & Fu, Q. (2021). Aerosol Direct Radiative Effects at the ARM SGP and TWP Sites: Clear Skies. *Journal of Geophysical Research: Atmospheres*, 126(5), e2020JD033663.

Yamaguchi, T., Feingold, G., & Kazil, J. (2019). Aerosol-cloud interactions in trade wind cumulus clouds and the role of vertical wind shear. *Journal of Geophysical Research: Atmospheres*, 124(22), 12244-12261.

Zieger, P., Fierz-Schmidhauser, R., Gysel, M., Ström, J., Henne, S., Yttri, K. E., ... &

Weingartner, E. J. A. C. (2010). Effects of relative humidity on aerosol light scattering in the Arctic. *Atmospheric Chemistry and Physics*, 10(8), 3875-3890.

Zieger, P., Väisänen, O., Corbin, J. C., Partridge, D. G., Bastelberger, S., Mousavi-Fard, M., ... & Salter, M. E. (2017). Revising the hygroscopicity of inorganic sea salt particles. *Nature Communications*, 8(1), 1-10.

## APPENDIX A

Table A1. Model summary of the 3D shortwave radiative transfer emulator in chapter 2.

Layer	Output shape	Param #	Connected to	Other information
Input_1	(None, 75, 75, 150, 2)	0	-	-
Conv3d_1	(None, 69, 69, 2, 64)	940,928	Input_1	64 filters with the size of (7, 7, 150) ; stride is (1, 1, 1), and no padding
Conv3d_2	(None, 67, 67, 2, 12)	147,712	Conv2d_1	128 filters with the size of (3, 3, 1) ; stride is (1, 1, 1), and no padding
Flatten_1	(None, 1149184)	0	Conv2d_2	-
Dense_1	(None, 128)	147,095,680	Flatten_1	128 neurons
Dense_2	(None, 128)	16,512	Dense_1	128 neurons
Dense_3	(None, 128)	16,512	Dense_2	128 neurons
Dense_4	(None, 128)	16,512	Dense_3	128 neurons
Dense_5	(None, 128)	16,512	Dense_4	128 neurons
Dense_6	(None, 128)	16,512	Dense_5	128 neurons
Dense_7	(None, 128)	16,512	Dense_6	128 neurons
Dense_8	(None, 128)	16,512	Dense_7	128 neurons
Dense_9	(None, 300)	38,700	Dense_8	reshape the output into two profiles (downwelling and upwelling)

Total parameters: 148,338,604; trainable parameters: 148,338,604; non-trainable parameters: 0

We used Glorot uniform initializer for the weights and zero initializer for the biases. The batch size for training is 64 samples, and the model learns the relationship between inputs and outputs by fitting the entire training dataset 50 times (i.e., epoch is 50). The testing loss continued to lower down throughout the entire training process (i.e., no sign of overfitting), so no regularization techniques were implemented. This specific architecture is based a series of trial-and-error as well as some fundamental knowledge of 3D radiative transfer (e.g., the output domain has to be smaller than the input domain).

Table A2. Model summary of the new aerosol retrieval method in chapter 3.

Layer	Output shape	Param #	Connected to	Other information
Input_1	(None, 45, 45, 1)	0	-	-
Conv2d_1	(None, 41, 41, 64)	1664	Input_1	64 filters with the size of (5, 5) ; stride is (1,1), and no padding
Conv2d_2	(None, 39, 39, 128)	73856	Conv2d_1	128 filters with the size of (3, 3) ; stride is (1,1), and no padding
Flatten_1	(None, 194688)	0	Conv2d_2	-
Dense_1	(None, 1024)	199361536	Flatten_1	1024 neurons
Dense_2	(None, 625)	640625	Dense_1	reshape the output into a 25-by-25 2D map

Total parameters: 200,077,681; trainable parameters: 200,077,681; non-trainable parameters: 0

We used Glorot uniform initializer for the weights and zero initializer for the biases. The batch size for training is 64 samples, and the model learns the relationship between inputs and outputs by fitting the entire training dataset 50 times (i.e., epoch is 50). The testing loss continued to lower down throughout the entire training process (i.e., no sign of overfitting), so no regularization techniques were implemented.

## APPENDIX B

1D Radiative transfer calculation has been known to be notoriously expensive in the modeling community, and is even more under a 3D environment. In our study, to calculate the shortwave broadband flux for a single snapshot and one single solar position with 16 cores of CPU takes about 3 days (equivalent to ~1000 core hours). With 279 snapshots and two solar positions in mind, that is a total of ~0.5M core hours, and no single cluster that I was aware of can afford this amount of computing. We sought different resources (Asha owned by College of Engineering at CSU, Summit owned by University of Colorado at Boulder, Stratus owned by Atmospheric Radiation Measurement under the Department of Energy, Casper and Summit owned by National Center for Atmospheric Research; a total of 5 clusters) to complete the task, but still fall short eventually given the limited time I have for my Master degree.